The Influence of Turbulence Memory on Idealized Tornado Simulations

AARON WANG,[a] YING PAN,[a] AND PAUL M. MARKOWSKI[a]

[a] *The Pennsylvania State University, University Park, Pennsylvania*

(Manuscript received 30 January 2020, in final form 17 September 2020)

ABSTRACT: Surface friction contributes to tornado formation and maintenance by enhancing the convergence of angular momentum. The traditional lower boundary condition in atmospheric models typically assumes an instant equilibrium between the unresolved stress and the resolved shear. This assumption ignores the physics that turbulent motions are generated and dissipated at finite rates—in effect, turbulence has a memory through its lifetime. In this work, a modified lower boundary condition is proposed to account for the effect of turbulence memory. Specifically, when an air parcel moves along a curved trajectory, a normal surface-shear-stress component arises owing to turbulence memory. In the accompanying large-eddy simulation (LES) of idealized tornadoes, the normal surface-shear-stress component is a source of additional dynamic instability, which provides an extra pathway for the development of turbulent motions. The influence of turbulence memory on the intensity of quasi-steady-state tornadoes remains negligible as long as assumptions employed by the modified lower boundary condition hold over a relatively large fraction of the flow region of interest. However, tornadoes in a transient state may be especially sensitive to turbulence memory.

SIGNIFICANCE STATEMENT: Friction between the wind and the ground can influence atmospheric phenomena in important ways. For example, surface friction can be a significant source of rotation in some thunderstorms, and it can also help to intensify rotation when rotation is already present. Unfortunately, the representation of friction's effects in atmospheric simulations is especially error-prone in phenomena characterized by rapid temporal evolution or strong spatial variations. Our work explores a new framework for representing friction to include the effect of the so-called turbulence memory. The approach is tested in idealized tornado simulations, but it may be applied to a wide range of atmospheric vortices.

KEYWORDS: Turbulence; Surface layer; Tornadoes; Large-eddy simulations

1. Introduction

It is well known that surface friction, at least up to a point, can intensify vortices by preventing cyclostrophic balance (Fig. 1a) and promoting radial inflow, thereby promoting the convergence of angular momentum toward the axis of rotation (Burggraf et al. 1971; Lewellen 1976, 1993; Davies-Jones et al. 2001; Rotunno 2013; Schlichting and Gersten 2017). Friction retards the velocity of air parcels orbiting the axis of rotation, thereby weakening the centrifugal force acting on the air, leading to a net inward acceleration of air parcels toward the axis of rotation (Fig. 1b). If friction becomes excessive, however, the loss of angular momentum to the ground can overwhelm the radial flow of angular momentum toward the axis, thereby weakening the vortex.

It is traditionally assumed that the surface friction is directed opposite the near-surface velocity, with its magnitude being proportional to the product of the wind speed squared and a drag coefficient. However, this assumption ignores the fact that friction really is manifest through the actions of turbulent eddies. Turbulent motions are generated and dissipated at finite rates—in effect, turbulence (and friction) has a *memory* through its lifetime. Because of the memory of turbulence, a more realistic treatment of the effects of turbulent mixing and friction should not constrain the friction to be opposite the velocity vector, particularly in the strongly curved flows of a vortex. In this article we will demonstrate a simple way of accounting for the memory of turbulence in strongly curved flow.

In the opening paragraph, the inward acceleration of air parcels is brought about not by an inward-directed friction force, but because of the effect of friction in weakening the outward-directed centrifugal force. In this article it will be shown that an *inward-directed* friction force acts on air parcels in a vortex (either cyclonic or anticyclonic) when the memory of turbulence is accounted for. On one hand, the inward-directed friction force potentially could enhance the convergence of angular momentum toward the axis of rotation, leading to stronger vortices and/or more rapid vortex formation. On the other hand, if the magnitude of the friction force is enhanced, vortex weakening is a possibility. These two possibilities will be explored via idealized numerical simulations of tornadoes.

The approach that is used to account for the memory of turbulence is presented in section 2. The configuration and results of the aforementioned numerical simulations of tornadoes are presented in sections 3 and 4, respectively. Conclusions are presented in section 5.

2. Accounting for the memory of turbulence in lower boundary condition

a. *Inconsistency between the traditional lower boundary condition and the nonzero turbulence lifetime*

The traditional lower boundary condition[1] (also known as a semi-slip lower boundary condition) in atmospheric models

Corresponding author: Ying Pan, yyp5033@psu.edu

---

[1] The lower boundary condition here is often termed a "wall model" in the engineering community, in which the walls are not limited to the bottom of the domain (e.g., pipe flow). Pope (2000, p. 443 and p. 634) provides expressions of the traditional lower boundary condition for RANS and LES, respectively.

DOI: 10.1175/MWR-D-20-0031.1

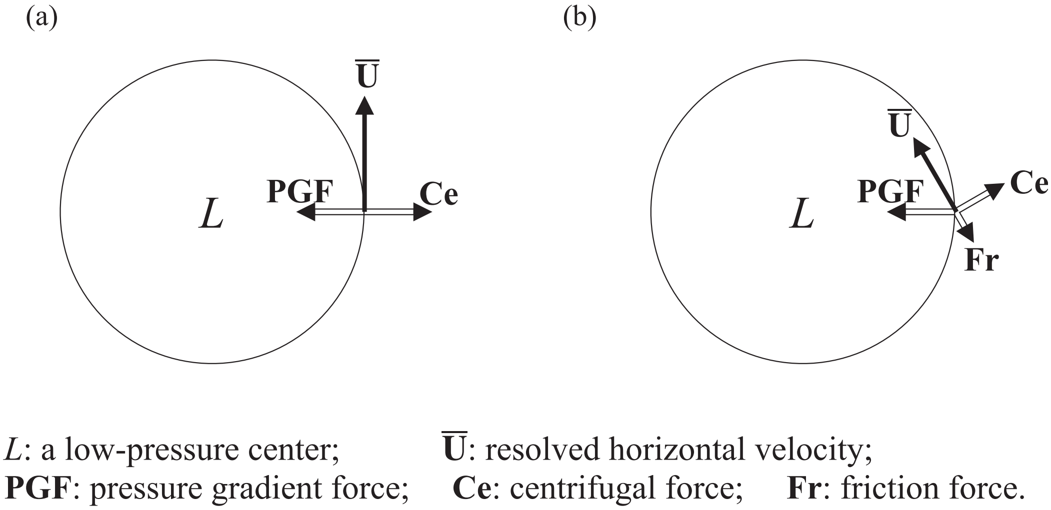

FIG. 1. A diagram showing the force balance of a cyclostrophic flow (a) without surface friction [similar to Fig. 3.4 in Holton and Hakim (2013)] and (b) with surface friction.

assumes that the kinematic shear stress at the lower boundary ($\boldsymbol{\tau}_w = \mathbf{i}\tau_{xz} + \mathbf{j}\tau_{yz}$) is opposite the resolved, first-grid-level horizontal velocity ($\overline{\mathbf{U}}_1 = \mathbf{i}\overline{u}_1 + \mathbf{j}\overline{v}_1$):

$$\boldsymbol{\tau}_w = -u_*^2 \frac{\overline{\mathbf{U}}_1}{\overline{U}_1}. \tag{1}$$

Here u_* is the friction velocity defined as the square root of the magnitude of $\boldsymbol{\tau}_w$, $\overline{U}_1$ is the magnitude of $\overline{\mathbf{U}}_1$, and $\mathbf{i}$ and $\mathbf{j}$ are zonal and meridional unit vectors, respectively. For large-eddy simulations (LES), the overbar represents a spatial filtering, whereas for Reynolds-averaged Navier–Stokes (RANS) simulations, the overbar represents an ensemble average. Equation (1) can be rewritten as

$$\boldsymbol{\tau}_w = -\frac{u_*}{\overline{U}_1} u_* z_1 \frac{\overline{\mathbf{U}}_1}{z_1}, \tag{2}$$

where z_1 is the first-grid-level height. Equation (2) suggests that the relationship between the unresolved stress ($\boldsymbol{\tau}_w$) and resolved strain rate ($\overline{\mathbf{U}}_1/z_1$) is characterized by a scalar, $-(u_*/\overline{U}_1)(u_* z_1)$, which has the same dimensions as kinematic viscosity. Thus, (1) is an eddy-viscosity model that assumes an instant equilibrium between unresolved stress and resolved strain rate, implying that unresolved turbulent motions are generated at a rate much faster than the rate of change of resolved motions (assumptions and potential issues associated with eddy-viscosity models are discussed in detail by Davidson 2015, 169–171).

However, turbulence is always generated and dissipated at finite rates, corresponding to a nonzero lifetime. According to Richardson's concept of energy cascade, the lifetime of a turbulent eddy is of the order of the so-called turnover time computed as the ratio between characteristic length and velocity scales (ℓ and u, respectively; see Davidson 2015, p. 24). These characteristic scales are essential ingredients of empirical flux–profile relationships like the Monin–Obukhov similarity theory [MOST, proposed by Monin and Obukhov (1954)]. MOST is applicable to statistically steady, horizontally homogeneous, fully developed, shear-dominated turbulent flows above a rigid, flat, rough surface. If shear-production and viscous dissipation of turbulent kinetic energy (TKE) are in approximate balance, then mean shear ($\partial\overline{U}/\partial z$) and viscous dissipation ε are characterized by the same velocity and length scales (u and ℓ, respectively).

Dimensional analysis suggests that the dimensionless shear,

$$\phi_m = \frac{\kappa z}{u_*}\frac{\partial \overline{U}}{\partial z} = \frac{\kappa z}{u_*}\frac{u}{\ell}, \tag{3}$$

and the dimensionless viscous dissipation rate,

$$\phi_\epsilon = \frac{\kappa z}{u_*^3}\epsilon = \frac{\kappa z}{u_*^3}\frac{u^3}{\ell}, \tag{4}$$

where $\kappa = 0.4$ is the von Kármán constant. Combining (3) and (4) suggests that MOST turbulence is characterized by a velocity scale,

$$u = u_*\left(\frac{\phi_\epsilon}{\phi_m}\right)^{1/2}, \tag{5}$$

and a length scale,

$$\ell = \kappa z \frac{\phi_\epsilon^{1/2}}{\phi_m^{3/2}}. \tag{6}$$

The turbulence turnover time is given by

$$\mathcal{T}_T = \frac{\ell}{u} = \frac{\kappa z}{u_* \phi_m}, \tag{7}$$

which characterizes how fast eddies of size ℓ pass most of their energy onto smaller structures (Davidson 2015, p. 25), meaning how fast old turbulence is replaced by new turbulence.

For shear-dominated turbulent flows, $\mathcal{T}_T$ can also be introduced using velocity and length scales associated with only the shear production of TKE, which are the friction velocity u_* and the Prandtl's mixing length ℓ_m, respectively. The Prandtl's mixing length model uses a scalar eddy viscosity ν_T to characterize the relationship between unresolved stress and resolved local strain:

$$u_*^2 = \nu_T \frac{\partial \overline{U}}{\partial z}, \tag{8}$$

where the eddy viscosity is formulated as (Davidson 2015, p. 113)

$$\nu_T = \ell_m^2 \left| \frac{\partial \overline{U}}{\partial z} \right|, \tag{9}$$

in which $\partial \overline{U}/\partial z$ is always positive near the surface, and therefore the absolute-value operator can be dropped.

Combining the MOST dimensionless shear (3) with (8) and (9) yields

$$\ell_m = \frac{u_*}{\partial \overline{U}/\partial z} = \frac{\kappa z}{\phi_m}, \tag{10}$$

which then yields

$$\mathcal{T}_T = \frac{\ell_m}{u_*} = \frac{\kappa z}{u_* \phi_m}. \tag{11}$$

Because u_* and ℓ_m are velocity and length scales associated with only shear production of TKE, $\mathcal{T}_T$ is a time scale related to shear production of TKE. The coincidence that $\mathcal{T}_T = \ell/u = \ell_m/u_*$ is reasonable because MOST is applicable to only shear-dominated turbulent flows. In other words, $\mathcal{T}_T$ also characterizes how fast unresolved turbulence adjusts to changes in resolved motions.

The assumption of an instant equilibrium between surface shear stress $\boldsymbol{\tau}_w$ and near-surface shear $(\overline{\mathbf{U}}_1/z_1)$ required by (1) is unphysical because of the finite rate of energy cascade. Appropriate modification to (1), which, in component form, is

$$\boldsymbol{\tau}_{xz} = -u_*^2 \frac{\overline{u}_1}{\overline{U}_1} \quad \text{and} \tag{12}$$

$$\boldsymbol{\tau}_{yz} = -u_*^2 \frac{\overline{v}_1}{\overline{U}_1}, \tag{13}$$

is needed to account for the effects of the nonzero turbulence lifetime.

b. A modified lower boundary condition accounting for turbulence memory associated with the curvature of an air parcel's trajectory

Accounting for the turbulence lifetime requires investigating the history of turbulence statistics. The evolution of the kinematic stress tensor $\boldsymbol{\tau}$ is governed by

$$\frac{\overline{D}\boldsymbol{\tau}}{Dt} = \frac{\partial \boldsymbol{\tau}}{\partial t} + \overline{\mathbf{u}} \cdot \nabla \boldsymbol{\tau} = \mathbf{P} + \mathbf{T} + \mathbf{R} + \mathbf{C} + \mathbf{B} + \mathbf{D}, \tag{14}$$

where $\overline{D}/Dt$ represents the rate of change of any flow property following an air parcel moving with the resolved velocity $\overline{\mathbf{u}}$ (Pope 2000, p. 84). Here $\nabla = \mathbf{i}(\partial/\partial x) + \mathbf{j}(\partial/\partial y) + \mathbf{k}(\partial/\partial z)$ and $\overline{\mathbf{u}} = \mathbf{i}\overline{u} + \mathbf{j}\overline{v} + \mathbf{k}\overline{w}$, where $\mathbf{i}$, $\mathbf{j}$, and $\mathbf{k}$ are unit vectors in the zonal (x), meridional (y), and vertical (z) directions, respectively. The right-hand-side (rhs) terms are the shear production $\mathbf{P}$, turbulent transport $\mathbf{T}$, pressure-gradient interaction $\mathbf{R}$, Coriolis effect $\mathbf{C}$, buoyancy contribution $\mathbf{B}$, and viscous dissipation $\mathbf{D}$. Wyngaard (2010, p. 188) provides the component form of (14) with a mathematical expression for each term. Integrating (14) from an arbitrary reference time t_0 to the current time t yields

$$\begin{aligned}\boldsymbol{\tau}(t) = &\int_{t_0}^{t} \mathbf{P}\,dt' + \int_{t_0}^{t} \mathbf{T}\,dt' + \int_{t_0}^{t} \mathbf{R}\,dt' + \int_{t_0}^{t} \mathbf{C}\,dt' \\ &+ \int_{t_0}^{t} \mathbf{B}\,dt' + \int_{t_0}^{t} \mathbf{D}\,dt' + \boldsymbol{\tau}(t_0).\end{aligned} \tag{15}$$

Any turbulence property at t_0 should have been completely dissipated after a sufficiently long time period of integration, $(t - t_0) \sim 10\mathcal{T}_L$. Here $\mathcal{T}_L$ is the Lagrangian integral time scale that measures the "memory" of an air parcel's Lagrangian velocity fluctuation (see definition in Wyngaard 2010, p. 82).

For shear-dominated turbulent flows, once $\boldsymbol{\tau}(t)$ no longer depends on $\boldsymbol{\tau}(t_0)$, $\boldsymbol{\tau}(t)$ can be modeled as a time-integration of $\mathbf{P}(t')$ modulated by the other terms on the rhs of (14) over the period between t' and t. The simplest relationship between $\boldsymbol{\tau}(t)$ and $\mathbf{P}(t')$ can be represented using a second-order tensor, $\mathbf{F}(t, t')$, which represents influences of turbulent transport, pressure-gradient interaction, Coliolis acceleration, buoyancy, and viscous dissipation during the period between t' and t. The kinematic stress tensor is therefore modeled as

$$\boldsymbol{\tau}(t) = \int_{t_0}^{t} \mathbf{F}(t,t') \cdot \mathbf{P}(t')\,dt'. \tag{16}$$

Combining (16) and the relationship,

$$\boldsymbol{\tau}(t) \cdot \mathbf{k} = \mathbf{i}\tau_{xz}(t) + \mathbf{j}\tau_{yz}(t) + \mathbf{k}\tau_{zz}(t), \tag{17}$$

yields

$$\boldsymbol{\tau}_w(t) = \mathbf{i}\tau_{xz}(t) + \mathbf{j}\tau_{yz}(t) = \int_{t_0}^{t} \mathbf{F}(t,t') \cdot \mathbf{P}(t') \cdot \mathbf{k}\,dt' - \mathbf{k}\tau_{zz}(t). \tag{18}$$

The expression for shear production is

$$\mathbf{P}(t') = -[\nabla \overline{\mathbf{u}}(t')]^{\mathrm{T}} \cdot \boldsymbol{\tau}(t') - \boldsymbol{\tau}(t') \cdot [\nabla \overline{\mathbf{u}}(t')], \tag{19}$$

where the superscript T represents the transpose of a second-order tensor. If viscous dissipation is a dominant mechanism to balance shear production of turbulence, then $\mathbf{F}(t, t')$ is approximately isotropic, that is,

$$\mathbf{F}(t,t') \approx F(t,t')\boldsymbol{\delta}, \tag{20}$$

where $\boldsymbol{\delta}$ is the Kronecker delta, and $F(t, t')$ is a scalar. Combining (18), (19), and (20) yields

$$\begin{aligned}\boldsymbol{\tau}_w(t) = &-\mathbf{i}\int_{t_0}^{t} F(t,t')\left(\tau_{xz}\frac{\partial \overline{u}}{\partial x}+\tau_{yz}\frac{\partial \overline{u}}{\partial y}+\tau_{zz}\frac{\partial \overline{u}}{\partial z}+\tau_{xx}\frac{\partial \overline{w}}{\partial x}+\tau_{xy}\frac{\partial \overline{w}}{\partial y}+\tau_{xz}\frac{\partial \overline{w}}{\partial z}\right)dt' \\ &-\mathbf{j}\int_{t_0}^{t} F(t,t')\left(\tau_{xz}\frac{\partial \overline{v}}{\partial x}+\tau_{yz}\frac{\partial \overline{v}}{\partial y}+\tau_{zz}\frac{\partial \overline{v}}{\partial z}+\tau_{yx}\frac{\partial \overline{w}}{\partial x}+\tau_{yy}\frac{\partial \overline{w}}{\partial y}+\tau_{yz}\frac{\partial \overline{w}}{\partial z}\right)dt' \\ &-\mathbf{k}\left[\int_{t_0}^{t} F(t,t')\left(\tau_{xz}\frac{\partial \overline{w}}{\partial x}+\tau_{yz}\frac{\partial \overline{w}}{\partial y}+\tau_{zz}\frac{\partial \overline{w}}{\partial z}+\tau_{zx}\frac{\partial \overline{w}}{\partial x}+\tau_{zy}\frac{\partial \overline{w}}{\partial y}+\tau_{zz}\frac{\partial \overline{w}}{\partial z}\right)dt'+\tau_{zz}(t)\right]. \qquad (21)\end{aligned}$$

Because $\boldsymbol{\tau}_w(t)$ consists of only horizontal components by definition, the vertical component on the rhs of (21) has to vanish. Without prior knowledge of external forcing terms that drive the atmospheric turbulence, one can assume that the kinematic stress tensor components are of the same order of magnitude. The resolved velocity ($\overline{\mathbf{u}}$) at the first grid level z_1 is usually approximately horizontal, meaning that horizontal velocity and length scales are typically much larger than vertical velocity and length scales, respectively. Scale analysis at z_1 suggests that terms associated with vertical gradients of horizontal resolved velocity components $[(\partial\overline{u}/\partial z)$ and $(\partial\overline{v}/\partial z)]$ are much larger than the other terms in horizontal components on the rhs of (21). We then simplify (21) as

$$\begin{aligned}\boldsymbol{\tau}_w(t) &\approx -\mathbf{i}\int_{t_0}^{t} F(t,t')\tau_{zz}(t')\frac{\partial \overline{u}_1(t')}{\partial z}dt' - \mathbf{j}\int_{t_0}^{t} F(t,t')\tau_{zz}(t')\frac{\partial \overline{v}_1(t')}{\partial z}dt' \\ &= -\int_{t_0}^{t} F(t,t')\tau_{zz}(t')\frac{\partial[\mathbf{i}\overline{u}_1(t')+\mathbf{j}\overline{v}_1(t')]}{\partial z}dt' \\ &= -\int_{t_0}^{t} F(t,t')\tau_{zz}(t')\frac{\partial \overline{\mathbf{U}}_1(t')}{\partial z}dt', \qquad (22)\end{aligned}$$

which implies that the contribution of shear production to $\boldsymbol{\tau}_w(t)$ during an infinitesimal time step dt' is approximately opposite the resolved first-grid-level horizontal velocity $[\overline{\mathbf{U}}_1(t')]$.

Assuming that the resolved velocity at the first grid level is predominantly horizontal ($\overline{\mathbf{u}}_1 \approx \overline{\mathbf{U}}_1$), we can define a natural coordinate system for an air parcel following the resolved motion in a horizontal plane (Fig. 2). The longitudinal and normal unit vectors are defined as $\mathbf{s}(t) = \overline{\mathbf{U}}_1(t)/\overline{U}_1(t)$ and $\mathbf{n}(t) = \mathbf{k} \times \mathbf{s}(t)$, respectively. The traditional lower boundary condition (1) assumes that $\boldsymbol{\tau}_w(t)$ is opposite to $\mathbf{s}(t)$, meaning no surface-shear-stress component in the normal direction $[\boldsymbol{\tau}_w(t) \cdot \mathbf{n}(t) = 0]$. The model (22) built upon the evolution equation for kinematic stress tensor, however, suggests that the surface-shear-stress component in the normal direction is not necessarily zero.

Specifically, we can use the first-order approximation of resolved first-grid-level horizontal velocity,

$$\overline{\mathbf{U}}_1(t') \approx \overline{\mathbf{U}}_1(t) - (t-t')\overline{\mathbf{a}}_1(t), \qquad (23)$$

as long as $\mathcal{O}\{[\overline{\mathbf{U}}_1(t) - \overline{\mathbf{U}}_1(t')]/\overline{\mathbf{U}}_1(t)\} < \mathcal{O}(0.1)$, where $\mathcal{O}$ represents the order of magnitude, and $\overline{\mathbf{a}}_1$ is resolved horizontal acceleration at the first grid level z_1, the component form of which in the natural coordinate system is

$$\overline{\mathbf{a}}_1 = \mathbf{s}\frac{D\overline{U}_1}{Dt} + \mathbf{n}\frac{\overline{U}_1^2}{R_s}, \qquad (24)$$

where R_s is the curvature radius of the resolved trajectory. In atmospheric models, R_s can be computed using resolved first-grid-level horizontal velocity ($\overline{\mathbf{U}}_1$) and acceleration ($\overline{\mathbf{a}}_1$). Specifically, the normal component of resolved acceleration can be obtained from

$$\mathbf{n} \cdot \overline{\mathbf{a}}_1 = (\mathbf{k} \times \mathbf{s}) \cdot \overline{\mathbf{a}}_1 = \mathbf{k} \cdot (\mathbf{s} \times \overline{\mathbf{a}}_1). \qquad (25)$$

Combining (24), (25), and $\mathbf{s} = \overline{\mathbf{U}}_1/\overline{U}_1$ yields

$$R_s = \frac{\overline{U}_1^3}{\mathbf{k} \cdot (\overline{\mathbf{U}}_1 \times \overline{\mathbf{a}}_1)}. \qquad (26)$$

Combining (22) and (23) yields the longitudinal component of $\boldsymbol{\tau}_w(t)$,

$$\begin{aligned}\tau_s(t) &= \boldsymbol{\tau}_w(t) \cdot \mathbf{s}(t) \\ &\approx -\int_{t_0}^{t} F(t,t')\tau_{zz}(t')\frac{\partial[\overline{\mathbf{U}}_1(t) - (t-t')\overline{\mathbf{a}}_1(t)]}{\partial z}dt' \cdot \mathbf{s}(t) \\ &= -\int_{t_0}^{t} F(t,t')\tau_{zz}(t')\frac{\partial[\overline{U}_1(t)\mathbf{s}(t)\cdot\mathbf{s}(t) - (t-t')\overline{\mathbf{a}}_1(t)\cdot\mathbf{s}(t)]}{\partial z}dt' \\ &= -\int_{t_0}^{t} F(t,t')\tau_{zz}(t')\frac{\partial(\overline{U}_1)}{\partial z}dt' + \int_{t_0}^{t} F(t,t')\tau_{zz}(t')\frac{\partial[(t-t')\overline{\mathbf{a}}_1(t)\cdot\mathbf{s}(t)]}{\partial z}dt' \\ &= -\frac{\partial[\overline{U}_1(t)]}{\partial z}\int_{t_0}^{t} F(t,t')\tau_{zz}(t')\,dt' + \frac{\partial[\overline{\mathbf{a}}_1(t)\cdot\mathbf{s}(t)]}{\partial z}\int_{t_0}^{t} F(t,t')\tau_{zz}(t')(t-t')\,dt', \qquad (27)\end{aligned}$$

and the normal component of $\boldsymbol{\tau}_w(t)$,

$$\begin{aligned}
\tau_n(t) &= \boldsymbol{\tau}_w(t)\cdot\mathbf{n}(t)\\
&\approx -\int_{t_0}^{t} F(t,t')\tau_{zz}(t')\frac{\partial[\overline{\mathbf{U}}_1(t)-(t-t')\overline{\mathbf{a}}_1(t)]}{\partial z}\,dt'\cdot\mathbf{n}(t)\\
&= -\int_{t_0}^{t} F(t,t')\tau_{zz}(t')\frac{\partial[\overline{U}_1(t)\mathbf{s}(t)\cdot\mathbf{n}(t)-(t-t')\overline{\mathbf{a}}_1(t)\cdot\mathbf{n}(t)]}{\partial z}\,dt'\\
&= \int_{t_0}^{t} F(t,t')\tau_{zz}(t')\frac{\partial[(t-t')\overline{\mathbf{a}}_1(t)\cdot\mathbf{n}(t)]}{\partial z}\,dt'\\
&= \frac{\partial[\overline{\mathbf{a}}_1(t)\cdot\mathbf{n}(t)]}{\partial z}\int_{t_0}^{t} F(t,t')\tau_{zz}(t')(t-t')\,dt'. \qquad (28)
\end{aligned}$$

The implication of (27) and (28) is consistent with the lag of the shear stress behind mean shear in a pressure-driven three-dimensional boundary layer observed in wind tunnel experiments (e.g., Bradshaw and Pontikos 1985) and direct numerical simulations (e.g., Moin et al. 1990). Field data frequently report nonnegligible surface-shear-stress component in the transverse direction of mean shear (e.g., Mahrt et al. 2001; Pan and Patton 2017), although direct measurements of acceleration are unavailable.

In the absence of resolved acceleration (i.e., $\overline{\mathbf{a}}_1 = 0$ for any time), $\boldsymbol{\tau}_w = \mathbf{s}\tau_s + \mathbf{n}\tau_n$ must recover the traditional lower boundary condition (1). Therefore we have

$$-u_*^2 \approx -\frac{\partial[\overline{U}_1(t)]}{\partial z}\int_{t_0}^{t} F(t,t')\tau_{zz}(t')\,dt', \qquad (29)$$

where u_* is the friction velocity computed for the traditional lower boundary condition.

Scale analysis suggests that

$$\begin{aligned}
\mathcal{O}\left[\frac{|\tau_s-(-u_*^2)|}{u_*^2}\right] &\sim \mathcal{O}\left\{\frac{\dfrac{\partial[\overline{\mathbf{a}}_1(t)\cdot\mathbf{s}(t)]}{\partial z}\displaystyle\int_{t_0}^{t} F(t,t')\tau_{zz}(t')(t-t')\,dt'}{\dfrac{\partial[\overline{U}_1(t)]}{\partial z}\displaystyle\int_{t_0}^{t} F(t,t')\tau_{zz}(t')\,dt'}\right\}\\
&\sim \mathcal{O}\left\{\frac{\displaystyle\int_{t_0}^{t} F(t,t')\tau_{zz}(t')\frac{\partial[(t-t')\overline{\mathbf{a}}_1(t)\cdot\mathbf{s}(t)]}{\partial z}\,dt'}{\dfrac{\partial[\overline{U}_1(t)]}{\partial z}\displaystyle\int_{t_0}^{t} F(t,t')\tau_{zz}(t')\,dt'}\right\} < \mathcal{O}\left\{\frac{\displaystyle\int_{t_0}^{t} F(t,t')\tau_{zz}(t')\frac{\partial[(t-t')|\overline{\mathbf{a}}_1(t)|]}{\partial z}\,dt'}{\dfrac{\partial[\overline{U}_1(t)]}{\partial z}\displaystyle\int_{t_0}^{t} F(t,t')\tau_{zz}(t')\,dt'}\right\}\\
&\sim \mathcal{O}\left\{\frac{\displaystyle\int_{t_0}^{t} F(t,t')\tau_{zz}(t')\frac{\partial[|\overline{U}_1(t)-\overline{U}_1(t')|]}{\partial z}\,dt'}{\dfrac{\partial[\overline{U}_1(t)]}{\partial z}\displaystyle\int_{t_0}^{t} F(t,t')\tau_{zz}(t')\,dt'}\right\} < \mathcal{O}\left\{\frac{\displaystyle\int_{t_0}^{t} F(t,t')\tau_{zz}(t')\frac{\partial[0.1|\overline{U}_1(t)|]}{\partial z}\,dt'}{\dfrac{\partial[\overline{U}_1(t)]}{\partial z}\displaystyle\int_{t_0}^{t} F(t,t')\tau_{zz}(t')\,dt'}\right\}\\
&\sim \mathcal{O}\left\{\frac{0.1\left|\dfrac{\partial[\overline{U}_1(t)]}{\partial z}\right|\displaystyle\int_{t_0}^{t} F(t,t')\tau_{zz}(t')\,dt'}{\left|\dfrac{\partial[\overline{U}_1(t)]}{\partial z}\right|\displaystyle\int_{t_0}^{t} F(t,t')\tau_{zz}(t')\,dt'}\right\} \sim \mathcal{O}(0.1) \quad \text{and}\\
\mathcal{O}\left[\frac{|\tau_n|}{u_*^2}\right] &\sim \mathcal{O}\left\{\frac{\dfrac{\partial[\overline{\mathbf{a}}_1(t)\cdot\mathbf{n}(t)]}{\partial z}\displaystyle\int_{t_0}^{t} F(t,t')\tau_{zz}(t')(t-t')\,dt'}{\dfrac{\partial[\overline{U}_1(t)]}{\partial z}\displaystyle\int_{t_0}^{t} F(t,t')\tau_{zz}(t')\,dt'}\right\}\\
&\sim \mathcal{O}\left\{\frac{\displaystyle\int_{t_0}^{t} F(t,t')\tau_{zz}(t')\frac{\partial[(t-t')\overline{\mathbf{a}}_1(t)\cdot\mathbf{n}(t)]}{\partial z}\,dt'}{\dfrac{\partial[\overline{U}_1(t)]}{\partial z}\displaystyle\int_{t_0}^{t} F(t,t')\tau_{zz}(t')\,dt'}\right\} < \mathcal{O}\left\{\frac{\displaystyle\int_{t_0}^{t} F(t,t')\tau_{zz}(t')\frac{\partial[(t-t')|\overline{\mathbf{a}}_1(t)|]}{\partial z}\,dt'}{\dfrac{\partial[\overline{U}_1(t)]}{\partial z}\displaystyle\int_{t_0}^{t} F(t,t')\tau_{zz}(t')\,dt'}\right\} \sim \mathcal{O}(0.1), \qquad (30)
\end{aligned}$$

where the first-order approximation (23) has been applied. The scale analysis (30) shows that the modulation of the longitudinal component of surface shear stress $[\boldsymbol{\tau}_w(t)\cdot\mathbf{s}(t)]$ due to the longitudinal component of the resolved acceleration $[\overline{\mathbf{a}}_1(t)\cdot\mathbf{s}(t)]$ can be neglected in (27), because it is an order of magnitude smaller than the other term. Combining (27), (29), and (30) suggests that

$$\tau_s(t) \approx -u_*^2. \qquad (31)$$

In the presence of nonzero normal component of resolved acceleration $[\overline{\mathbf{a}}_1(t)\cdot\mathbf{n}(t)]$, (28) suggests that surface shear stress has a nonzero normal component $[\boldsymbol{\tau}_w(t)\cdot\mathbf{n}(t)]$, whose sign is the same as the normal component of resolved acceleration. We can use the first-order approximation of the angle between $\overline{\mathbf{U}}_1(t')$ and $\overline{\mathbf{U}}_1(t)$,

$$\theta(t,t') \approx (t-t')\frac{\overline{U}_1(t)}{R_s(t)}, \qquad (32)$$

as long as $\mathcal{O}[\theta(t, t')] < \mathcal{O}(0.1)$. Combining (24), (28), and (32) yields

$$\begin{aligned}\boldsymbol{\tau}_n(t) &\approx \frac{\partial}{\partial z}\left\{\frac{[\overline{U}_1(t)]^2}{R_s(t)}\right\}\int_{t_0}^{t} F(t,t')\boldsymbol{\tau}_{zz}(t')\theta(t,t')\frac{R_s(t)}{\overline{U}_1(t)}dt \\ &= \frac{\partial}{\partial z}\left\{\frac{[\overline{U}_1(t)]^2}{R_s(t)}\right\}\frac{R_s(t)}{\overline{U}_1(t)}(t-t_0)F(t,t_c)\boldsymbol{\tau}_{zz}(t_c)\theta(t,t_c),\end{aligned} \tag{33}$$

where t_c is a flow-dependent time between t_0 and t. The assumption that stress components are primarily modulated by viscous dissipation also implies that $F(t, t')$ tends to decay exponentially in time,

$$F(t,t') \approx \exp\left[-\gamma_0\frac{(t-t')}{\mathcal{T}_L}\right], \tag{34}$$

where γ_0 is a flow-dependent dimensionless coefficient, and $\mathcal{T}_L$ is the Lagrangian integral time scale. Because $\mathcal{T}_L$ is defined based upon a second-order autocorrelation function and $\boldsymbol{\tau}$ consists of only second-order turbulence statistics, γ_0 should be of the order of 1.

Combining (33) and (34) yields

$$\begin{aligned}\boldsymbol{\tau}_n(t) &\approx \frac{\partial}{\partial z}\left\{\frac{[\overline{U}_1(t)]^2}{R_s(t)}\right\}\frac{R_s(t)}{\overline{U}_1(t)}(t-t_0)\boldsymbol{\tau}_{zz}(t_c)\theta(t,t_c)\exp\left[-\gamma_0\theta(t,t_c)\frac{R_s(t)/\overline{U}_1(t)}{\mathcal{T}_L}\right] \\ &= \frac{\partial}{\partial z}\left\{\frac{[\overline{U}_1(t)]^2}{R_s(t)}\right\}\frac{R_s(t)}{\overline{U}_1(t)}(t-t_0)\boldsymbol{\tau}_{zz}(t_c)|\theta(t,t_c)|\frac{\theta(t,t_c)}{|\theta(t,t_c)|}\exp\left[-\gamma_0|\theta(t,t_c)|\frac{\mathcal{T}_T}{\mathcal{T}_L}\frac{\mathcal{T}_{TN}}{\mathcal{T}_T}\frac{|R_s(t)|/\overline{U}_1}{\mathcal{T}_{TN}}\right].\end{aligned} \tag{35}$$

Here $\mathcal{T}_T$ is the turbulence turnover time, and $\mathcal{T}_{TN} = \kappa z_1/u_*$ is the turnover time at the first grid level in statistically steady, horizontally homogeneous, neutrally stratified (for which the subscript "N" stands), fully developed turbulent flow above a rigid, flat, rough surface (hereinafter referred to as "an idealized surface layer"). Note that (32) suggests that $\theta(t, t')$ and $R_s(t)$ has the same sign, and therefore in (35) we have replaced $\theta(t, t_c)R_s(t)$ with $|\theta(t, t_c)||R_s(t)|$ within the exponential function. The acceleration of an air parcel along a curved trajectory is characterized by a time scale

$$\mathcal{T}_R = \frac{|R_s|}{\overline{U}_1} = \frac{\overline{U}_1^2}{|\overline{\mathbf{U}}_1 \times \overline{\mathbf{a}}_1|}, \tag{36}$$

where (26) has been used.

Combining (26) and (32) yields

$$\begin{aligned}\theta(t,t_c) &\approx (t-t_c)\frac{\overline{U}_1(t)}{R_s(t)} = (t-t_c)\frac{\overline{U}_1(t)}{[\overline{U}_1(t)]^3}\mathbf{k}\cdot[\overline{\mathbf{U}}_1(t)\times\overline{\mathbf{a}}_1(t)] \\ &= (t-t_c)\frac{\overline{U}_1(t)}{[\overline{U}_1(t)]^3}\mathbf{k}\cdot[\overline{U}_1(t)\mathbf{s}(t)\times\overline{\mathbf{a}}_1(t)] \\ &= (t-t_c)\frac{[\overline{U}_1(t)]^2}{[\overline{U}_1(t)]^3}[\mathbf{k}\times\mathbf{s}(t)]\cdot\overline{\mathbf{a}}_1(t) \\ &= \frac{(t-t_c)}{\overline{U}_1(t)}\mathbf{n}(t)\cdot\overline{\mathbf{a}}_1(t),\end{aligned} \tag{37}$$

meaning that the sign of $\theta(t, t_c)$ is the same as the sign of $\mathbf{n}(t)\cdot\overline{\mathbf{a}}_1(t)$. In other words, we have

$$\frac{\theta(t,t_c)}{|\theta(t,t_c)|} = \frac{\mathbf{n}(t)\cdot\overline{\mathbf{a}}_1(t)}{|\mathbf{n}(t)\cdot\overline{\mathbf{a}}_1(t)|}. \tag{38}$$

Scale analysis of terms in (35) suggests that

$$\begin{aligned}&\mathcal{O}\left(\frac{\partial}{\partial z}\left\{\frac{[\overline{U}_1(t)]^2}{R_s(t)}\right\}\right) \sim \mathcal{O}(u^2\ell^{-1}|R_s|^{-1}), \\ &\mathcal{O}\left[\frac{R_s(t)}{\overline{U}_1(t)}\right] \sim \mathcal{O}(|R_s|u^{-1}), \\ &\mathcal{O}[(t-t_0)] < \mathcal{O}(10\mathcal{T}_L) \sim \mathcal{O}\left(10\frac{\mathcal{T}_L}{\mathcal{T}_T}\mathcal{T}_T\right) \\ &\qquad \sim 10\mathcal{O}\left(\frac{\mathcal{T}_L}{\mathcal{T}_T}\right)\mathcal{O}(\ell u^{-1}), \\ &\mathcal{O}[\tau_{zz}(t_c)] \sim \mathcal{O}(u^2), \\ &\mathcal{O}[\theta(t,t_c)] \sim \mathcal{O}[\theta(t,t')] < \mathcal{O}(0.1), \\ &\mathcal{O}(\gamma_0) \sim \mathcal{O}(1), \\ &\mathcal{O}(u_*^2) \sim \mathcal{O}(u^2),\end{aligned} \tag{39}$$

where u and ℓ are characteristic velocity and length scales of turbulence.

The ratio $\mathcal{T}_T/\mathcal{T}_L$ accounts for the difference between turbulence turnover time (which assumes approximate balance between shear production and viscous dissipation of TKE) and Lagrangian integral time scale (which measures the memory of turbulence following an air parcel). For statistically homogeneous and isotropic turbulence that has no memory ($\mathcal{T}_L \rightarrow 0$), and therefore $\tau_n \rightarrow 0$, meaning that the traditional lower boundary condition given by (12) and (13) is recovered. For typical atmospheric turbulence, the Lagrangian integral time scale $\mathcal{T}_L$ is on the order of the Eulerian integral time scale $\mathcal{T}_E$, which measures the "memory" of the Eulerian velocity fluctuation at a fixed point (Wyngaard 2010, p. 36). Although no simple relationship exists between $\mathcal{T}_T$ and $\mathcal{T}_E$, we can assume that they are of the same order of magnitude. Therefore we have

$$\mathcal{O}(\mathcal{T}_T/\mathcal{T}_L) \sim \mathcal{O}(1). \tag{40}$$

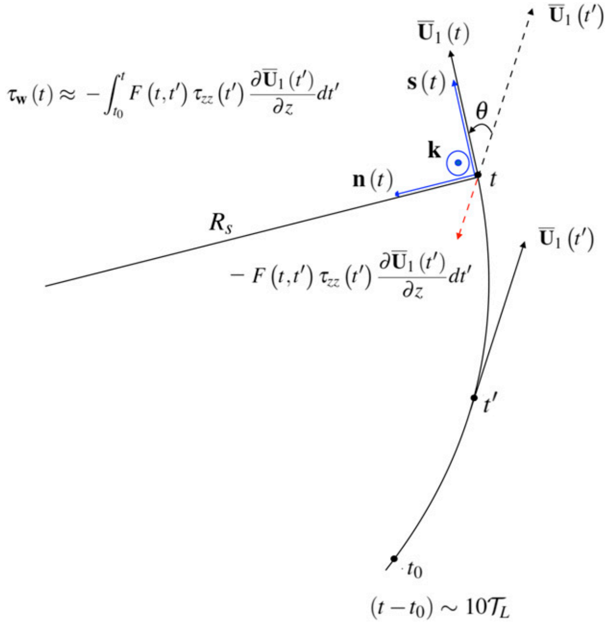

FIG. 2. A diagram showing surface shear stress $\boldsymbol{\tau}_w$ exerted on an air parcel moving with the resolved velocity at the first grid level, given by (22), which is an integration over a time period from t_0 to t. The resolved first-grid-level velocity is assumed to be approximately horizontal ($\overline{\mathbf{u}}_1 \approx \overline{\mathbf{U}}_1$) so that the air parcel's trajectory remains in a horizontal plane at the first grid level. Blue arrows represent unit vectors in a natural coordinate system following the air parcel's trajectory. The red dashed arrow represents the contribution of shear production to $\boldsymbol{\tau}_w$ during an infinitesimal time step dt', which is opposite $\overline{\mathbf{U}}_1(t')$. The red dashed arrow reveals that the change in $\boldsymbol{\tau}_w$ direction lags behind the change in $\overline{\mathbf{U}}_1$ direction, which introduces an inward-directed surface-shear-stress component as an air parcel's trajectory curves.

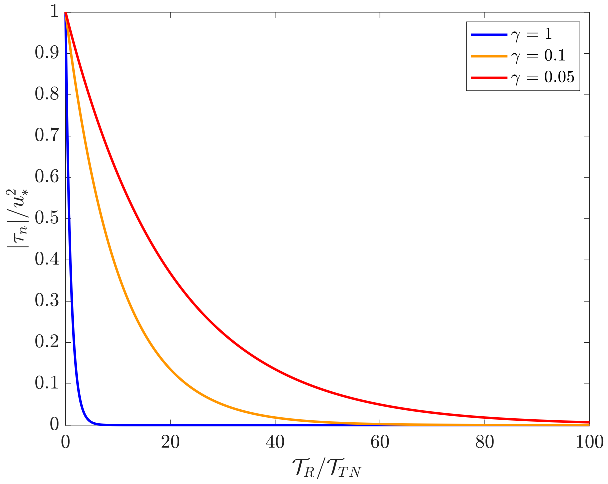

FIG. 3. The exponentially decaying rate of the effect of turbulence memory ($|\tau_n|/u_*^2$) vs the ratio of the curvature's characteristic time scale ($\mathcal{T}_R$) to turbulence lifetime ($\mathcal{T}_{TN}$) for different values of γ.

The ratio $\mathcal{T}_{TN}/\mathcal{T}_T$ accounts for the variation of turbulence turnover time due to environmental conditions that deviate from an idealized surface layer. Within the MOST framework, the Wangara Experiment data suggest that $0.4 \leq \phi_m \leq 6$ for $-2 \leq z/\mathcal{L} \leq 1$ (where $\mathcal{L}$ is the Obukhov length, which characterizes the influence of buoyancy; Kaimal and Finnigan 1994, 16–18), meaning that the turnover time (7) can vary between 0.17 and 2.5 times $\mathcal{T}_{TN}$. As mentioned in section 2a, the turnover time $\mathcal{T}_T$ is equivalent to the shear-production time scale ℓ_m/u_*. In the presence of canopies (e.g., plants and buildings), the canopy-shear-layer length scale (i.e., mean velocity divided by mean shear at canopy top) characterizes shear production. Laboratory and field experiment data suggest that the canopy-shear-layer length scale ranges from 0.12 to 0.85 the canopy height (e.g., Table 1 in Raupach et al. 1996). Given the same characteristic velocity scale, the turnover time can range from 0.3 to 2.1 times $\mathcal{T}_{TN}$. Within an idealized surface layer, u_* remains approximately constant with height, and therefore $\mathcal{T}_{TN} = \kappa z/u_*$ decreases with decreasing height. Within a canopy, the shear-production length scale ℓ_m typically remains approximately constant with height (see Fig. 6b in Poggi et al. 2004), whereas the friction velocity u_* decreases dramatically with decreasing height (see Fig. 1b in Raupach et al. 1996). Therefore $\mathcal{T}_T = \ell_m/u_*$ within a canopy increases with decreasing height. The opposite variations of $\mathcal{T}_{TN}$ and within-canopy $\mathcal{T}_T$ with height implies that the difference between $\mathcal{T}_{TN}$ and $\mathcal{T}_T$ within a canopy can be even larger than the difference at canopy top. Combining the presence of canopy and atmospheric stability can easily lead to a ratio $\mathcal{T}_{TN}/\mathcal{T}_T$ ranging from 0.1 to 10. Accounting for the effects of the other environmental conditions (e.g., surface heterogeneity, baroclinicity, and nonstationarity) may further increase the variability of $\mathcal{T}_{TN}/\mathcal{T}_T$. For shear-dominated atmospheric turbulent flows, we can assume that

$$\mathcal{O}(\mathcal{T}_{TN}/\mathcal{T}_T) < \mathcal{O}(10). \tag{41}$$

Combining (35), (38), (39), (40), and (41) suggests that

$$\tau_n \approx u_*^2 \frac{\mathbf{n}\cdot\overline{\mathbf{a}}_1}{|\mathbf{n}\cdot\overline{\mathbf{a}}_1|}\alpha \exp\left(-\gamma\frac{\mathcal{T}_R}{\mathcal{T}_{TN}}\right), \tag{42}$$

where α and γ are flow-dependent positive dimensionless numbers:

$$\begin{aligned}\alpha &= \frac{1}{u_*^2}\frac{\partial}{\partial z}\left\{\frac{[\overline{U}_1(t)]^2}{R_s(t)}\right\}\frac{R_s(t)}{\overline{U}_1(t)}(t-t_0)\tau_{zz}(t_c)|\theta(t,t_c)| \\ &< \mathcal{O}(u^{-2})\mathcal{O}(u^2\ell^{-1}|R_s|^{-1})\mathcal{O}(|R_s|u^{-1})10\mathcal{O}(1)(\ell u^{-1}) \\ &\quad \times \mathcal{O}(u^2)\mathcal{O}(0.1) \sim \mathcal{O}(1) \quad \text{and} \\ \gamma &= \gamma_0\theta(t,t_c)\frac{\mathcal{T}_T}{\mathcal{T}_L}\frac{\mathcal{T}_{TN}}{\mathcal{T}_T}\frac{R_s}{|R_s|} \\ &< \mathcal{O}(1)\mathcal{O}(0.1)\mathcal{O}(1)\mathcal{O}(10)\mathcal{O}(1) \\ &\sim \mathcal{O}(1).\end{aligned} \tag{43}$$

For the idealized study in this work, we specify $\alpha = 1$ and test three γ values: 1, 0.1, and 0.05. For the aforementioned idealized surface layer, $\mathcal{O}(\mathcal{T}_{TN}/\mathcal{T}_{T}) \sim \mathcal{O}(1)$, $\gamma = 0.1$. Decreasing γ increases the turbulence memory, which increases the influence of trajectory curvature on shear stresses. On the other hand, larger γ reduces the turbulence memory. Corresponding values of $|\tau_n|/u_*^2$ against $\mathcal{T}_R/\mathcal{T}_{TN}$ are shown in Fig. 3. Note that the first-order approximation (23) leads to $|\tau_n|/u_*^2 < \mathcal{O}(0.1)$ according to scale analysis (30).

The modified lower boundary condition is

$$\begin{aligned}
\tau_{xz} &= \mathbf{i}\cdot\boldsymbol{\tau}_w = \mathbf{i}\cdot(\mathbf{s}\tau_s + \mathbf{n}\tau_n) = \tau_s(\mathbf{i}\cdot\mathbf{s}) + \tau_n(\mathbf{i}\cdot\mathbf{n}) \\
&= \tau_s(\mathbf{i}\cdot\mathbf{s}) + \tau_n[\mathbf{i}\cdot(\mathbf{k}\times\mathbf{s})] \\
&= \tau_s(\mathbf{i}\cdot\mathbf{s}) + \tau_n[(\mathbf{i}\times\mathbf{k})\cdot\mathbf{s}] \\
&= \tau_s(\mathbf{i}\cdot\mathbf{s}) + \tau_n(-\mathbf{j}\cdot\mathbf{s}) \\
&= \tau_s\frac{\overline{u}_1}{\overline{U}_1} - \tau_n\frac{\overline{v}_1}{\overline{U}_1} \quad \text{and} \qquad (44)
\end{aligned}$$

$$\begin{aligned}
\tau_{yz} &= \mathbf{j}\cdot\boldsymbol{\tau}_w = \mathbf{j}\cdot(\mathbf{s}\tau_s + \mathbf{n}\tau_n) = \tau_s(\mathbf{j}\cdot\mathbf{s}) + \tau_n(\mathbf{j}\cdot\mathbf{n}) \\
&= \tau_s(\mathbf{j}\cdot\mathbf{s}) + \tau_n[\mathbf{j}\cdot(\mathbf{k}\times\mathbf{s})] \\
&= \tau_s(\mathbf{j}\cdot\mathbf{s}) + \tau_n[(\mathbf{j}\times\mathbf{k})\cdot\mathbf{s}] \\
&= \tau_s(\mathbf{j}\cdot\mathbf{s}) + \tau_n(\mathbf{i}\cdot\mathbf{s}) \\
&= \tau_s\frac{\overline{v}_1}{\overline{U}_1} + \tau_n\frac{\overline{u}_1}{\overline{U}_1}, \qquad (45)
\end{aligned}$$

where τ_s and τ_n are given by (31) and (42), respectively. Table 1 summarizes all assumptions that have been employed to derive the modified lower boundary condition. Mathematically, a nonzero τ_n associated with a curved trajectory implies that the relationship between the unresolved stress ($\boldsymbol{\tau}_w = \mathbf{i}\tau_{xz} + \mathbf{j}\tau_{yz}$) and the resolved strain rate ($\overline{\mathbf{U}}_1/z_1$) is no longer characterized by a scalar. Physically, the modified lower boundary condition is no longer an eddy-viscosity model but rather is a pseudo-second-order-closure model based upon the evolution equation for kinematic stress tensor (14). The normal component of mean shear stress τ_n accounts for a nonlinear dependence (exponential decay in particular) of unresolved stress on the history of resolved strain rate (represented by acceleration). In the limit of a straight trajectory, $R_s \to \infty$, $\mathcal{T}_R \to \infty$, $\tau_n \to 0$, and the traditional lower boundary condition given by (12) and (13) is recovered.

3. Numerical simulation configuration

Simulations of idealized tornadoes in a dry atmosphere are conducted using Cloud Model 1 (CM1, release 19.6), a compressible nonhydrostatic model. Prognostic equations of three velocity components, potential temperature, and nondimensional pressure (see appendix of Bryan and Morrison 2012) are solved in a rotating frame of reference. All of the simulations employ an LES closure with a subgrid TKE parameterization scheme (Deardorff 1980). The ''Fiedler chamber'' approach (see Fig. 2 of Rotunno et al. 2016) is used to generate and sustain simulated tornadoes, where a steady updraft forcing is specified in the middle of a rotating domain (Fiedler 1995). Comparison to recent LES studies employing a similar approach (Bryan et al. 2017; Nolan et al. 2017) are used to put our results into context.

Each simulation employs a constant grid spacing within the lowest 1 km of a central $(4\,\mathrm{km})^2$ region in the middle of the domain, hereinafter referred to as the ''inner domain.'' Outside of the inner domain, the grid is stretched toward the lateral and upper boundaries. Two inner-domain grid spacings, 10 and 25 m, in both the horizontal and vertical dimensions, are evaluated in the current study.

Table 2 summarizes the similarities and distinctions between the current model configuration and those in Bryan et al. (2017) and Nolan et al. (2017). One difference between our simulation configuration and that of Bryan et al. (2017) and Nolan et al. (2017) is that their lateral boundaries were closed (rigid and free-slip), whereas ours are open (wave-radiating). Each simulation starts from a neutral (i.e., constant potential temperature) atmosphere at rest (i.e., zero velocity everywhere) at $t = 0$. For simulations in Table 3 whose names do not contain ''NOPERT,'' small random potential temperature perturbations (0.25-K amplitude) are imposed throughout the domain at $t = 0$, and along the lateral boundaries[2] for the duration of the simulations, in order to trigger turbulence. These simulations do not use the ''eddy injection'' method, which is a more complicated method to generate turbulence [employed by one simulation in Bryan et al. (2017) and all simulations in Nolan et al. (2017)]. The other simulations in Table 3, whose names contain ''NOPERT,'' are conducted without the potential temperature perturbations in the initial and lateral boundary conditions to assess the possible adverse effects of laminar flow on the LES (Markowski and Bryan 2016).

Along the bottom boundary, Bryan et al. (2017) and Nolan et al. (2017) employed the traditional boundary condition described in section 2a, whereas the present study conduct simulations using both the traditional and modified (section 2b) boundary conditions. In all simulations including those using the modified lower boundary condition, the friction velocity u_* is computed by integrating (3) within the MOST framework over height from a prescribed roughness length z_0 to the first-grid-level z_1 [see details in section 1.3.5 of Kaimal and Finnigan (1994)].[3] Simulations using the traditional lower boundary condition in the present study are configured to be most similar to the simulation without eddy-injection in Bryan et al. (2017). Differences in simulation results induced by different inner-domain grid spacing values $[(10\,\mathrm{m})^3$ and $(25\,\mathrm{m})^3$ in the current work and $5\,\mathrm{m} \times 5\,\mathrm{m} \times 2.5\,\mathrm{m}$ in Bryan et al. (2017)] can be interpreted based on the sensitivity of simulated tornadoes to grid resolution investigated by Nolan et al. (2017).

---

[2] Imposing random perturbations along the lateral boundaries requires a minor modification to the original CM1 code. Without this modification, unrealistic two-dimensional structures aligned with the low-level inflow to the tornado emanate from the lateral boundaries and can induce significant (and unrealistic) tornado drift away from the origin.

[3] The actual mathematical expression in CM1 corresponds to an integration from z_0 to $(z_1 + z_0)$ for numerical stability purposes [e.g., see details in section 2 of Bryan et al. (2017)].

TABLE 1. Assumptions made in section 2b to derive the modified lower boundary condition.

Assumption	Physical implication	Associated equations	Potential cases of violation
Turbulence statistics are well defined over the period $(t - t_0) \sim 10\mathcal{T}_L$	Any turbulence property at t_0 should have been completely dissipated after a sufficiently long period of integration from t_0 to t, so that $\boldsymbol{\tau}(t)$ does not depend on $\boldsymbol{\tau}(t_0)$	(15)	Any process having a lifetime that is comparable to or shorter than $\mathcal{T}_L$
The turbulent flow is shear dominated	$\boldsymbol{\tau}$ can be modeled as $\mathbf{P}$ modulated by the other mechanisms	(16)	Buoyancy, transport, or Coriolis plays an important role in the evolution of $\boldsymbol{\tau}$
The relationship between $\boldsymbol{\tau}$ and $\mathbf{P}$ can be characterized by a second-order tensor	The simplest possible relationship between two second-order tensors is considered	(16)	The most general relationship between two second-order tensors is a fourth-order tensor
Viscous dissipation is the dominant mechanism that balances shear production	$\mathbf{F}$ is approximately isotropic, and its magnitude tends to decay exponentially in time	(20), (34)	Shear production and viscous dissipation of the kinematic stress tensor are imbalanced
The kinematic stress tensor components are of the same order of magnitude, and horizontal velocity and length scales are much larger than vertical velocity and length scales	The vertical gradients of horizontal velocity components are dominant terms in the resolved strain rate tensor	(22)	External driving forces lead to particular kinematic stress tensors, or horizontal scales are comparable to or smaller than vertical scales (e.g., turbulent motions in the universal range handled by subgrid-scale models in LES)
$\mathcal{O}\{[\overline{\mathbf{U}}_1(t) - \overline{\mathbf{U}}_1(t')]/\overline{\mathbf{U}}_1(t)\} < \mathcal{O}(0.1)$, where t' is any time between t_0 and t	A first-order approximation is applicable to $\overline{\mathbf{U}}_1(t)$, and subsequent scale analysis yields (30) and (31)	(23)	The time scale that characterizes the evolution of resolved motions is comparable to or shorter than the lifetime of turbulence
The resolved velocity at the first grid level is predominantly horizontal ($\overline{\mathbf{u}}_1 \approx \overline{\mathbf{U}}_1$)	A natural coordinate system is defined for an air parcel following the resolved motion in a horizontal plane (Fig. 2)	(24), (25), and (26)	The flow is close to the axis of rotation or away from the surface
$\mathcal{O}[\theta(t, t')'] < \mathcal{O}(0.1)$, where t' is any time between t_0 and t	A first-order approximation is applicable to $\theta(t, t')$, and subsequent scale analysis yields (43)	(32)	The time scale that characterizes the curvature of resolved trajectories is comparable to or shorter than the lifetime of turbulence
$\mathcal{T}_L$, $\mathcal{T}_E$, and $\mathcal{T}_T$ are of the same order of magnitude	Subsequent scale analysis yields (43)	(40)	In the presence of imbalanced shear production and viscous dissipation of TKE, $\mathcal{T}_L$, and $\mathcal{T}_E$ can be substantially different from $\mathcal{T}_T$, because the definition of $\mathcal{T}_T$ assumes approximate balance between shear-production and viscous dissipation of TKE

TABLE 2. Simulation configurations of the current study and two recent studies.

Study	Current study	Bryan et al. (2017)	Nolan et al. (2017)
Domain size	24 km × 24 km × 15 km	40 km × 40 km × 15 km	40 km × 40 km × 15 km
Grid points	600 × 600 × 240 320 × 320 × 152	1120 × 1120 ×512	1920 × 1920 × 912 1120 × 1120 × 512 720 × 720 312 520 × 520 ×212
Inner-domain size	4 km × 4 km × 1 km	4 km × 4 km × 1 km	4 km × 4 km × 1 km
Inner-domain grid spacing	10 m × 10 m × 10 m 25 m × 25 m × 25 m	5 m × 5 m × 2.5 m	2.5 m × 2.5 m × 1.25 m 5 m × 5 m × 2.5 m 10 m × 10 m × 5 m 20 m × 20 m × 10 m
Lower boundary condition	Semi-slip (OLD-) Modified (NEW-)	Semi-slip	No-slip
Roughness length (z_0)	0.2 m	0.2 m	0.2 m
Lateral boundary condition	Open (with perturbation except for NOPERT)	Closed, free-slip	Closed, free-slip
Upper boundary Condition	Closed, free-slip	Closed, no-slip	Closed, no-slip
Rayleigh damping layer	Uppermost 7 km	Uppermost 7 km	Uppermost 7 km
Amplitude of updraft forcing	0.359 m s^{-2}	0.359 m s^{-2}	0.359 m s^{-2}
Coriolis parameter	5.334×10^{-4} s^{-1}	5.334×10^{-4} s^{-1}	5.334×10^{-4} s^{-1}
Eddy injection	No	Yes and no	Yes

We now explain the nomenclature used in the remainder of the paper when referring to the various simulations performed. Simulations using the traditional (modified) lower boundary conditions are designated as "OLD" ("NEW"). Simulations employing a 10-m (25 m) inner-domain grid spacing are designated as "DX10" ("DX25"). In simulations using the modified lower boundary condition and a value of γ that is less than 1 (i.e., $\gamma = 0.1$ or 0.05), the value of γ is appended to the name. Last, "NOPERT" is appended to names of simulations without small random perturbations to potential temperature's initial and lateral boundary conditions. A summary is provided in Table 3.

4. Results

a. Simulations employing the traditional lower boundary condition

A simulation is performed using the traditional lower boundary condition, (10 m)^3 inner-domain grid spacing, and random perturbations in both initial and lateral boundary conditions (OLD-DX10). The simulation configuration is most similar to the simulation without eddy-injection in Bryan et al. (2017). The instantaneous vertical velocity field during the quasi–steady state is turbulent (see Fig. 4a), similar to Fig. 7b

TABLE 3. List of the name, description, and quasi-steady-state statistics (in boldface font) of each simulation. The indices in order are as follows: OLD/NEW is traditional or modified lower boundary condition; DX10/DX25 is inner-domain grid spacing = 10 or 25 m; NOPERT is no random perturbation imposed into potential temperature's initial and lateral boundary conditions (otherwise the potential temperature field starts with initial random perturbations and runs with random perturbations at the lateral boundary); and γ0.1/γ0.05 is $\gamma = 0.1$ or 0.05 (otherwise, the modified lower boundary condition's γ is 1). Note that the traditional lower boundary condition has no γ, which is computed in the modified lower boundary condition only. The quasi-steady-state maximum tangential (u_θ), inflow ($-u_r$), and vertical (w) velocity components are computed every 1 min and then averaged over the last 1 h of each simulation.

Case	Lower boundary condition	Random perturbation	Inner-domain grid spacing	γ	Max u_θ (m s^{-1})	Max $-u_r$ (m s^{-1})	Max w (m s^{-1})	Fraction of inner-domain area associated with $\lvert\tau_n\rvert/u_*^2 > 0.1$
OLD-DX10	Traditional	Yes	(10 m)^3	—	**117.3**	**83.4**	**108.1**	—
OLD-DX10-NOPERT	Traditional	No	(10 m)^3	—	**91.9**	**65.8**	**64.3**	—
NEW-DX10	Modified	Yes	(10 m)^3	1	**118.4**	**84.1**	**107.9**	0.0097%
NEW-DX10-NOPERT	Modified	No	(10 m)^3	1	**120.2**	**85.1**	**107.9**	0.0093%
NEW-DX10-γ0.1	Modified	Yes	(10 m)^3	0.1	**118.3**	**84.1**	**107.3**	3.3%
NEW-DX10-γ0.05	Modified	Yes	(10 m)^3	0.05	**118.1**	**85.3**	**103.0**	23%
OLD-DX25	Traditional	Yes	(25 m)^3	—	**96.9**	**74.7**	**74.1**	—
OLD-DX25-NOPERT	Traditional	No	(25 m)^3	—	**72.0**	**54.9**	**42.2**	—
NEW-DX25	Modified	Yes	(25 m)^3	1	**94.5**	**72.5**	**73.6**	0.10%
NEW-DX25-NOPERT	Modified	No	(25 m)^3	1	**95.8**	**72.8**	**73.5**	0.10%
NEW-DX25-γ0.1	Modified	Yes	(25 m)^3	0.1	**97.7**	**74.8**	**79.0**	26%
NEW-DX25-γ0.05	Modified	Yes	(25 m)^3	0.05	**107.0**	**77.4**	**101.0**	67%

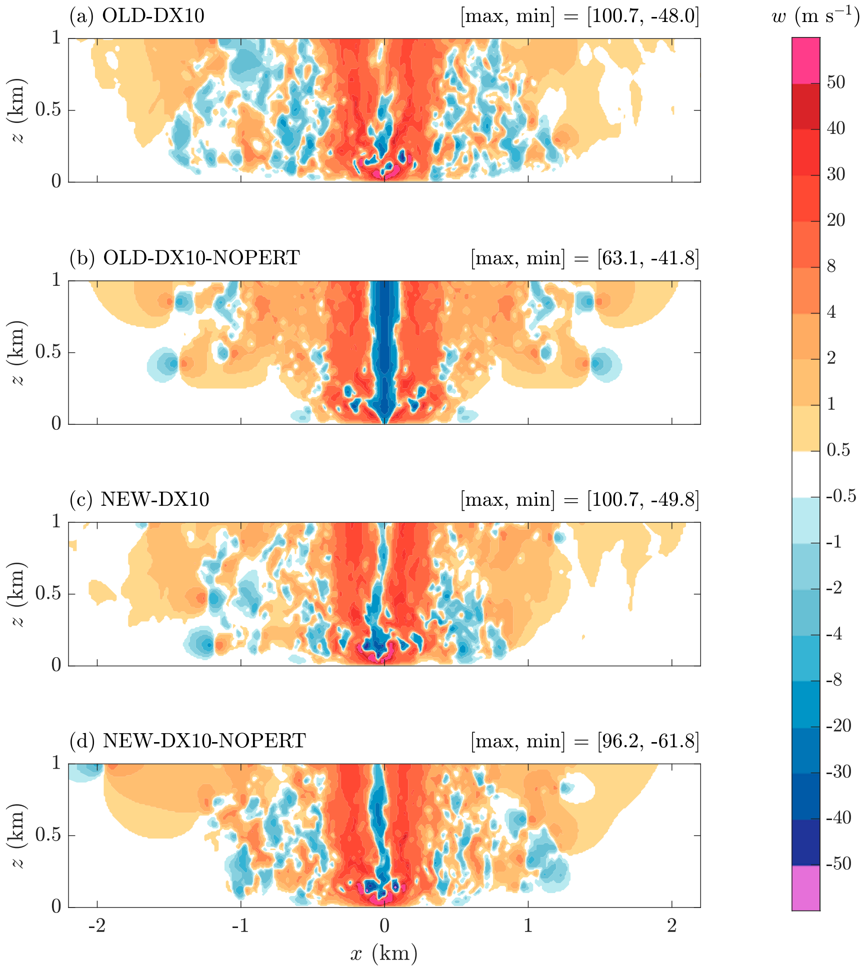

FIG. 4. Vertical velocity (color shading; m s^{-1}) at $t = 4$ h (quasi steady state) in four simulations using an inner-domain grid spacing of (10 m)^3 with both the traditional and modified lower boundary condition, with and without initial random temperature perturbations: (a) OLD-DX10, (b) OLD-DX10-NOPERT, (c) NEW-DX10, and (d) NEW-DX10-NOPERT.

in Bryan et al. (2017). The relatively fine inner-domain grid spacing used by Bryan et al. (2017) (5 m × 5 m × 2.5 m) yields finer-scale structures and larger vertical velocity variance (see maximum and minimum values annotated on associated figures) compared to OLD-DX10. The 5-min, time-azimuthal-averaged, quasi-steady-state wind field of simulation OLD-DX10 (Fig. 5a) is similar to Nolan et al. (2017)'s CTRL10 simulation, which used a similar inner-domain grid spacing (10 m × 10 m × 5 m) but with eddy-injection (see their Fig. 3b). OLD-DX10 yields a slightly stronger tornado than the CTRL10 simulation in Nolan et al. (2017), consistent with the understanding that eddy injection weakens a tornado (see Fig. 18 and associated discussion in Bryan et al. 2017).

Another simulation using the traditional lower boundary condition, (10 m)^3 inner-domain grid spacing, but without random perturbations in initial and lateral boundary conditions (OLD-DX10-NOPERT), is performed to investigate the sensitivity of simulated tornado to the imposed random perturbations. This simulation yields a laminar flow as characterized by an axisymmetric vertical velocity snapshot (Fig. 4b). The quasi-steady-state tornado vortex obtained using OLD-DX10-NOPERT is remarkably weaker than that obtained using OLD-DX10 (comparing OLD-DX10 and OLD-DX10-NOPERT in Table 3, Figs. 4a,b and 5a,b, respectively). The sensitivity of the simulation results to imposed random perturbations is expected for LES employing the traditional lower boundary condition, as reported by Markowski and Bryan (2016) based on LES of a neutral boundary layer.

b. *Simulations employing the modified lower boundary condition with $\gamma = 1$*

Specifying $\gamma = 1$ for the modified lower boundary condition described in section 2b and (41) means $\mathcal{O}(\mathcal{T}_{TN}/\mathcal{T}_T) \sim \mathcal{O}(10)$, implying that the time taken by unresolved surface shear stress to adjust to changes in resolved wind direction is shorter than the lifetime of turbulence in an idealized surface layer. A simulation using (10 m)^3 inner-domain grid spacing with random perturbations in both the initial and lateral

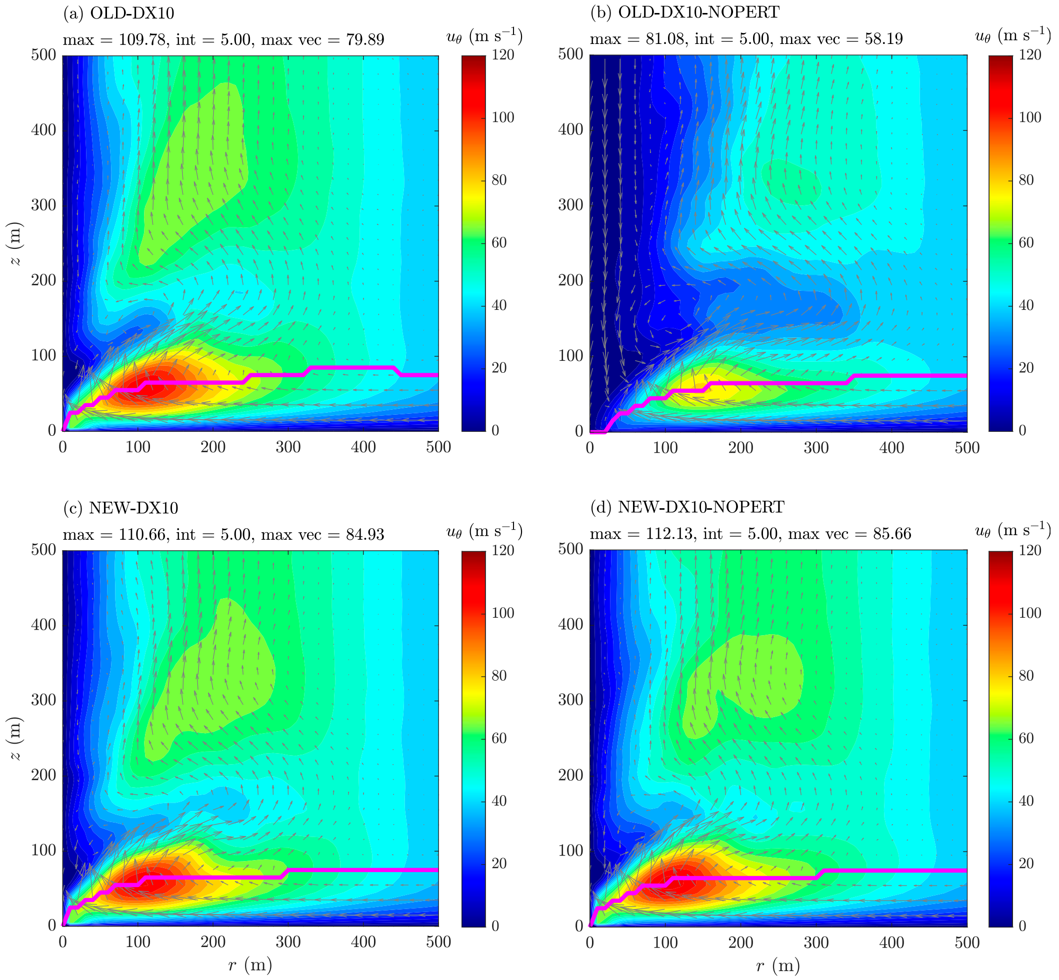

FIG. 5. Time- and azimuthally averaged mean wind fields in simulations (a) OLD-DX10, (b) OLD-DX10-NOPERT, (c) NEW-DX10, and (d) NEW-DX10-NOPERT. Gray vector arrows indicate radial and vertical velocity $[(u_r, w)]$. Shading is tangential velocity. The magenta line encloses the inflow layer, which is defined as the depth at which the inflow $(-u_r)$ is equal to 10% of the maximum inflow in that figure. For each of the panels, ''max'' indicates the maximum value of the shading, ''int'' indicates the interval of the shading, and ''max vec'' indicates the maximum magnitude of the vector. The time averaging is performed over $t \in$ [3 h 55 min, 4 h 0 min]. This figure can be compared with Fig. 5a in Nolan et al. (2017).

boundary conditions (NEW-DX10) yields results similar to those obtained using OLD-DX10 (cf. OLD-DX10 and NEW-DX10 in Table 3, Figs. 4a,c, and 5a,c). With $\gamma = 1$, accounting for the turbulence memory associated with curved trajectory has negligible influences on the statistics of the quasi-steady-state tornado.

Similar to the sensitivity study in section 4a, another simulation is performed using the modified lower boundary condition with $\gamma = 1$, $(10\,\mathrm{m})^3$ inner-domain grid spacing, but without random perturbations in the initial and lateral boundary conditions (NEW-DX10-NOPERT). Employing the modified lower boundary condition dramatically reduces the sensitivity of the simulated tornadoes to the imposed random perturbations (cf. NEW-DX10 and NEW-DX10-NOPERT in Table 3 and Figs. 4c,d, and 5c,d, respectively). Simulations performed using a coarser inner-domain grid spacing, $(25\,\mathrm{m})^3$, leads to the same conclusion that simulated tornadoes become much less sensitive to imposed random perturbations when one switches from the traditional lower boundary condition to the modified lower boundary condition with $\gamma = 1$ (cf. OLD-DX25, OLD-DX25-NOPERT, NEW-DX25, and NEW-DX-NOPERT in Table 3). When an air parcel changes direction on a horizontal plane at the first grid level, turbulence memory induces a normal surface-shear-stress component whose sign is the same as the sign of normal acceleration (42). The resulting normal surface-shear-stress component tends to pull the air parcel away from its original direction, implying that any small disturbance introduced into an air parcel's moving direction grows spontaneously, which satisfies the definition of dynamic instability (Holton and Hakim 2013, p. 213). The development of such dynamic instability provides a pathway for energy cascade from large to small scales. Employing the modified lower boundary condition ensures development of turbulent

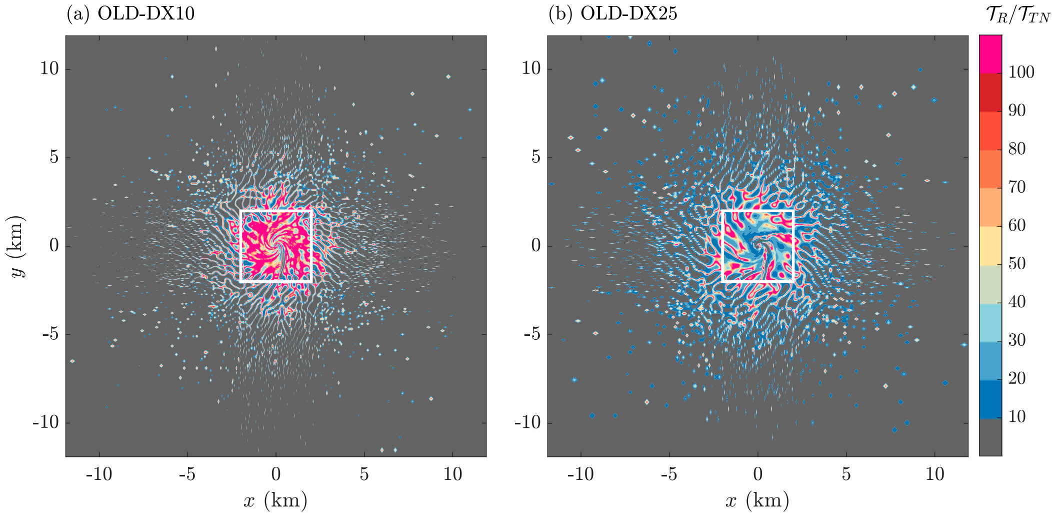

FIG. 6. The ratio of $\mathcal{T}_R$ to $\mathcal{T}_{TN}$ at $t = 4$ h (i.e., during the quasi steady state) in simulations using the traditional boundary condition and inner-domain grid spacings of $(10\,\mathrm{m})^3$ and $(25\,\mathrm{m})^3$: (a) OLD-DX10 and (b) OLD-DX25. The white squares mark the inner domain. Extremely large values (where turbulence memory is negligible) exceeding 100 are shaded magenta. Smaller $\mathcal{T}_R/\mathcal{T}_{TN}$ indicates a larger effect of turbulence memory (Fig. 3).

flow as long as the resolved flow field has curved trajectories, a condition easily satisfied in both the near-field and far-field environment of the tornadoes.

c. Sensitivity to variability in turbulence memory

For environmental flows in general, the time taken by unresolved stress to adjust to changes in resolved shear can easily vary by an order of magnitude (see discussion of $\mathcal{T}_{TN}/\mathcal{T}_T$ in section 2b). Scale analysis (43) suggests that $\gamma < 1$ may be more representative to typical atmospheric-surface-layer conditions than $\gamma = 1$. Decreasing γ increases the potential influence of turbulence memory, which may not be limited to only enhancing the instability development and energy cascade. We are particularly interested in whether the modified lower boundary condition with $\gamma < 1$ can intensify or weaken a tornado, which is a question raised in the introduction.

The sensitivity study consists of simulations performed using three choices of γ (1, 0.1, and 0.05) and two choices of inner-domain grid spacing, $(10\,\mathrm{m})^3$ and $(25\,\mathrm{m})^3$. Increasing the inner-domain grid spacing increases the energy carried by unresolved motions, and therefore increases the relative importance of changes made in the parameterization scheme that estimates unresolved surface shear stress. Mathematically, increasing z_1 (which equals half of the inner-domain grid spacing) increases $\mathcal{T}_{TN} = \kappa z_1/u_*$ and decreases $\mathcal{T}_R = |R_s|/\overline{U}_1$ (due to the increase of $\overline{U}_1$). Thus, different inner-domain grid spacing leads to different spatial distribution of $\mathcal{T}_R/\mathcal{T}_{TN}$. During quasi–steady state, tornadoes obtained using $(10\,\mathrm{m})^3$ inner-domain grid spacing show $\mathcal{T}_R/\mathcal{T}_{TN} > 100$ for the majority of the inner domain (the region inside the 4 km × 4 km white square in Fig. 6a), whereas tornadoes obtained using $(25\,\mathrm{m})^3$ inner-domain grid spacing show $\mathcal{T}_R/\mathcal{T}_{TN} < 40$ for a significant portion of the inner domain (region inside the 4 km × 4 km white square in Fig. 6b). Consequently, quasi-steady-state tornadoes obtained using the $(10\,\mathrm{m})^3$ inner-domain grid spacing show negligible sensitivity to the three choices of γ (cf. NEW-DX10, NEW-DX10-γ0.1, and NEW-DX10-γ0.05 in Table 3), whereas quasi-steady-state tornadoes obtained using a $(25\,\mathrm{m})^3$ inner-domain grid spacing show significant intensification when γ is reduced from 1 to 0.05 (cf. NEW-DX25, NEW-DX25-γ0.1, and NEW-DX25-γ0.05 in Table 3).

Because the derivation in section 2b employs a first-order approximation for $\overline{\mathbf{U}}_1$ (23), scale analysis (30) suggests that $|\tau_n|/u_*^2 < 0.1$ is required for the modified lower boundary condition to be applicable. Table 3 provides the fraction of inner-domain area associated with $|\tau_n|/u_*^2 > 0.1$ for each of the quasi-steady-state tornadoes obtained using the modified lower boundary condition. A negligible fraction (<5%) implies that the modified lower boundary condition is well applicable (e.g., NEW-DX10, NEW-DX10-γ0.1, and NEW-DX25), whereas an excessively large fraction (>50%) indicates potentially unphysical results (e.g., NEW-DX25-γ0.05). Table 3 suggests that quasi-steady-state tornadoes are insensitive to the choice of γ as long as the fraction of inner-domain area associated with $|\tau_n|/u_*^2 > 0.1$ is within 30%.

The 3-h spinup period of the simulations is also investigated to understand the influence of turbulence memory on tornado development. For each of the simulations using $(25\,\mathrm{m})^3$ inner-domain grid spacing, the tornado vortex intensity increases monotonically in its approach to the quasi–steady state, no matter whether the traditional or modified lower boundary conditions are applied, or what γ value is specified in the modified lower boundary condition (Fig. 7). However, this is not necessarily the case for simulations using $(10\,\mathrm{m})^3$ inner-domain grid spacing and the modified lower boundary condition. In the NEW-DX10-γ0.05 tornado, the maximum values of all three velocity components peak between $t = 1$ h and $t = 3$ h, then decrease to lesser quasi-steady-state values (Fig. 8). Although the applicability of the modified lower boundary condition to NEW-DX10-γ0.05 is somewhat questionable due

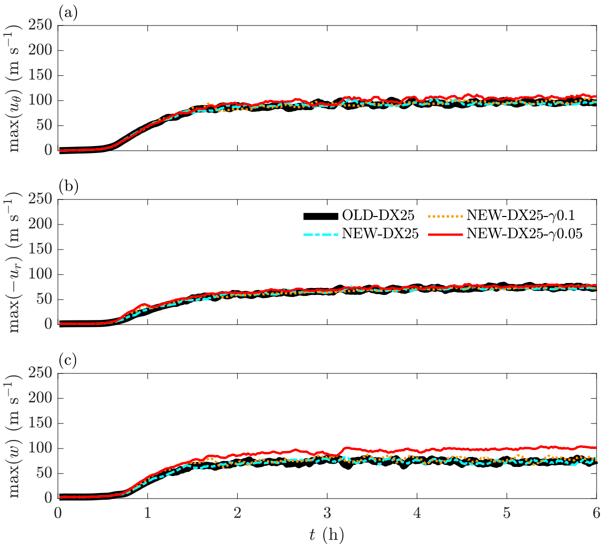

FIG. 7. Running 5-min averages of maximum (a) tangential velocity $\mathbf{u}_\theta$, (b) inflow velocity $-\mathbf{u}_r$, and (c) vertical velocity w for simulations OLD-DX25, NEW-DX25, NEW-DX25-γ0.1, and NEW-DX25-γ0.05.

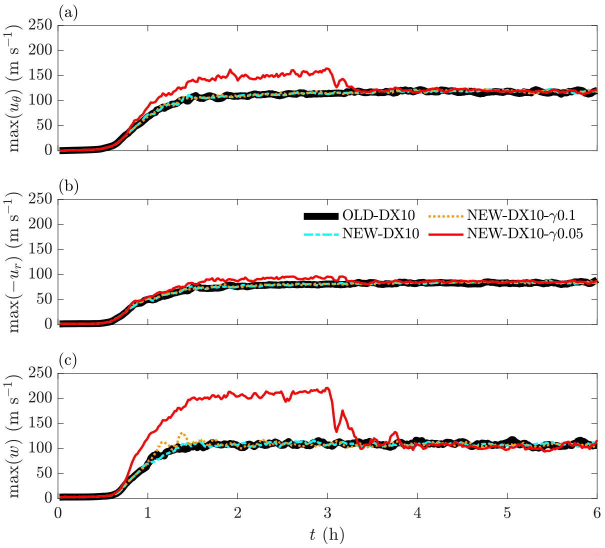

FIG. 8. As in Fig. 7, but for simulations OLD-DX10, NEW-DX10, NEW-DX10-γ0.1, and NEW-DX10-γ0.05.

to a nonnegligible fraction of inner-domain area associated with $|\tau_n|/u_*^2 > 0.1$ (23% in Table 3), results during the spinup period reveals interesting influence of turbulence memory on the evolution of tornado structure.

All quasi-steady-state tornadoes obtained in the present study (e.g., Fig. 4) and by Bryan et al. (2017) consist of a central downdraft. No central downdraft, however, presents at $t < 2$ h 25 min for NEW-DX10-γ0.05 (e.g., $t = 2$ h 15 min shown in Fig. 9a), when the tornado attains extreme vertical velocities [max(w) ≈ 200 m s^{-1}]. Over the next hour (2 h 25 min $< t <$ 3 h 25 min), the downdraft forms aloft and gradually extends toward the surface over the next hour (e.g., $t = 2$ h 40 min and 3 h 5 min shown in Figs. 9b,c, respectively). At $t >$ 3 h 25 min the tornado structure becomes similar to the quasi-steady-state structure in simulation NEW-DX10 (cf. Figs. 9d and 4c, both at $t = 4$ h). The region of most intense azimuthal wind becomes broader, shallower, and weaker as the central downdraft develops and extends toward the surface (Fig. 10). The tornado's evolution shown in Figs. 9 and 10 is an example of an initially low-swirl supercritical end-wall vortex capped by a descending vortex breakdown bubble that may eventually culminate in a two-cell structure if the axial downdraft descends all the way to the surface, which have been investigated from theoretical, laboratory, and numerical simulation perspectives (Church et al. 1977; Fiedler and Rotunno 1986; Lewellen and Lewellen 2007; Rotunno 2013; Davies-Jones 2015).

The central downdraft is formed by the development of downward-directed vertical pressure-gradient force along the axis, in conjunction with extremely low pressure just above the surface. The low pressure center is also linked to the inward-directed pressure gradient force that drives near-surface convergence. Turbulence memory associated with curved trajectories leads to an inward-directed surface-shear-stress component, which enhances near-surface convergence. In the early stage ($t <$ 3 h) of the NEW-DX10-γ0.05 simulation, the enhanced near-surface convergence due to turbulence memory intensifies the tornado noticeably faster than the development of a low pressure center near the surface. For example, at $t =$ 2 h approximately 40% of the inner-domain area is associated with $\mathcal{T}_R/\mathcal{T}_{TN} < 50$ (Fig. 11a) and correspondingly $|\tau_n|/u_*^2 > 0.1$ (can be inferred from Fig. 3). The tornado attains extreme velocities, while a central downdraft has not developed yet (Fig. 9a). During the period from $t = 2$ h to $t = 4$ h, values of $\mathcal{T}_R/\mathcal{T}_{TN}$ within the inner domain gradually increase with time (cf. Figs. 11a,b), which weaken the inward-directed surface shear stress associated with turbulence memory and favor the formation of central downdraft. Once the central downdraft forms, the tornado structure approaches a quasi steady state. The quasi-steady-state tornado with a central downdraft is much less intense than at earlier times prior to the development of a central downdraft.

5. Conclusions

The lower boundary condition traditionally employed in atmospheric models assumes an instantaneous equilibrium between unresolved stress at the lower boundary (i.e., surface friction) and the resolved strain rate between the lower boundary and the first grid level. Therefore, it neglects the nonzero lifetime of turbulence. In this work, a modified lower boundary condition was proposed to account for the effect of turbulence lifetime associated with curved trajectories. In a natural coordinate system following an air parcel moving with the resolved horizontal velocity at the first grid level, the surface shear stress has a nonzero normal component, in addition to the longitudinal component, which is approximately the same as the surface shear stress computed using the traditional lower boundary condition. A theoretical derivation starting

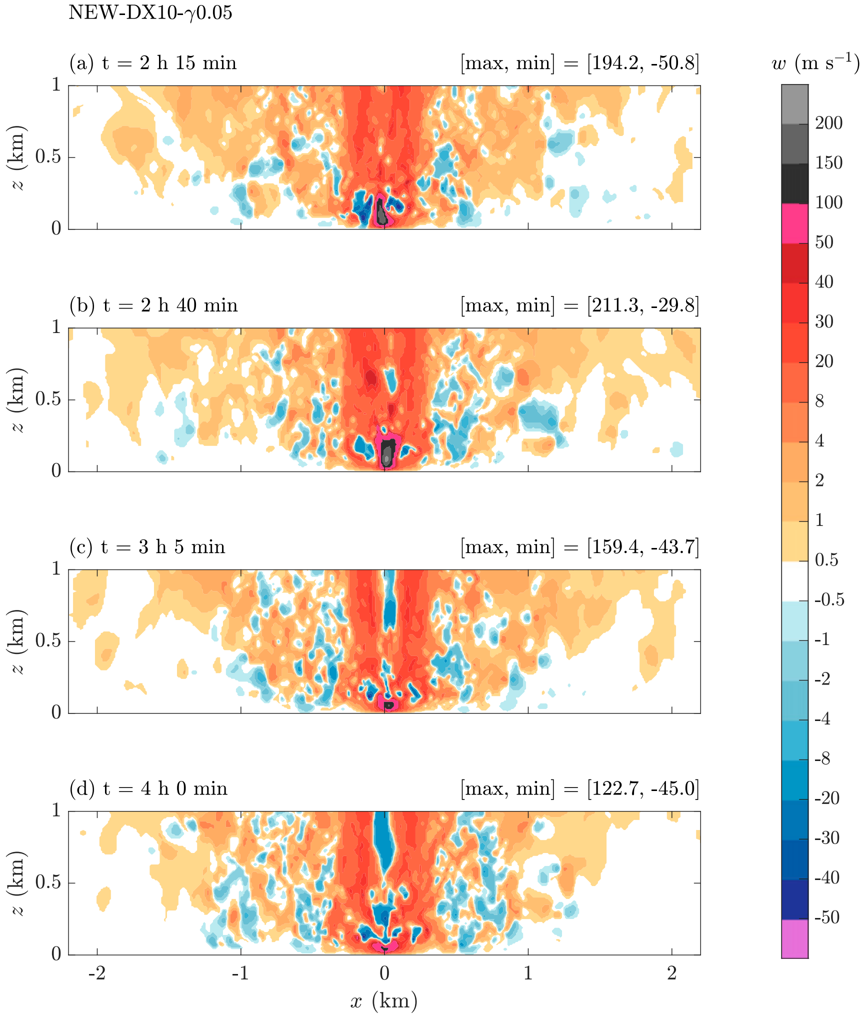

FIG. 9. As in Fig. 4, but for simulation NEW-DX10-γ0.05 at t = (a) 2 h 15 min, (b) 2 h 40 min, (c) 3 h 5 min, and (d) 4 h 0 min.

from the evolution equation for the kinematic stress tensor suggests that the normal component of surface shear stress has the same sign as that of the normal component of resolved horizontal acceleration at the first grid level. For an atmospheric vortex, the normal component of surface shear stress serves as an inward-directed friction force, which may strengthen the vortex by enhancing the convergence of angular momentum toward the axis rotation. On the other hand, the magnitude of surface shear stress computed using the modified lower boundary condition is always larger than that computed using the traditional lower boundary condition. Thus, the enhanced surface shear stress magnitude could potentially weaken a vortex. In addition, when an air parcel changes direction in a horizontal plane, the resulting surface shear stress tends to pull the air parcel farther away from its original direction. The positive feedback between the normal components of surface shear stress and resolved horizontal shear provides a pathway for dynamic instability development that is not captured by the traditional lower boundary condition.

The modified lower boundary condition was implemented into CM1 to examine potential influence of turbulence memory on idealized tornadoes. The simulations employed an LES closure, and tornadoes were generated and sustained using the "Fiedler Chamber" approach. Simulation results obtained using the traditional lower boundary condition were first compared with those of Bryan et al. (2017) and Nolan et al. (2017), who performed similar simulations. Simulations using the modified lower boundary condition were performed using arbitrarily specified parameters, $\alpha = 1$ and $\gamma = 1, 0.1$, and 0.05. Quantifying flow-dependent dimensionless positive numbers, α and γ, using field experimental data remains unfeasible owing to no direct measurements of acceleration and large uncertainties in surface shear stress estimates (often >20%). Nevertheless, scale analysis based upon assumptions made for the modified lower boundary condition suggests that $\alpha < \mathcal{O}(1)$ and $\gamma < \mathcal{O}(1)$. When compared with simulations using the traditional lower boundary condition, employing the modified lower boundary condition with $\gamma = 1$ has negligible influences

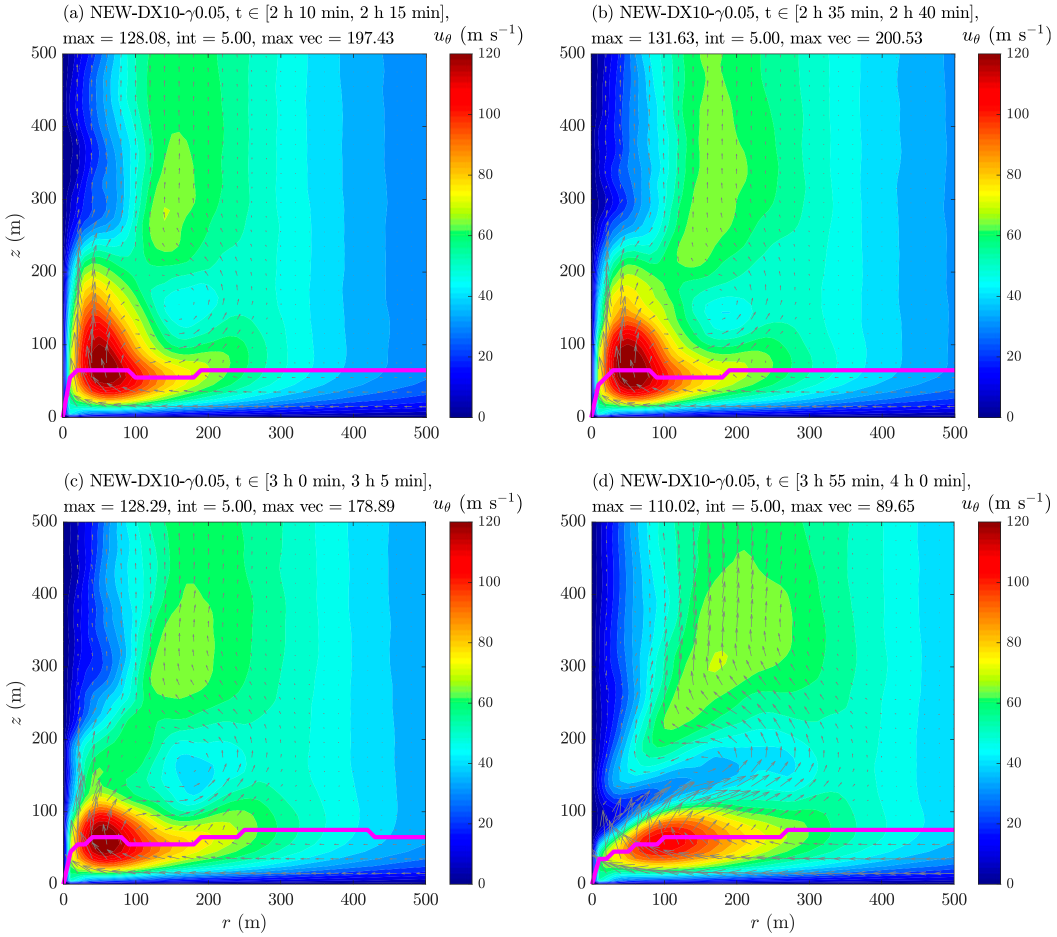

FIG. 10. As in Fig. 5, but for simulation NEW-DX10-γ0.05 averaged over $t \in$ (a) [2 h 10 min, 2 h 15 min], (b) [2 h 35 min, 2 h 40 min], (c) [3 h 0 min, 3 h 5 min], and (d) [3 h 55 min, 4 h 0 min].

on the simulated tornado as long as appropriate random perturbations are imposed via the initial and lateral boundary conditions to trigger turbulence. Without the imposed random perturbations, simulations using the modified lower boundary condition with $\gamma = 1$ continue to yield similar turbulent flow patterns, whereas simulations using the traditional lower boundary condition yields axisymmetric, laminar flows. The modified lower boundary condition is capable of triggering turbulence in the absence of imposed random perturbations because it provides an extra pathway for dynamic instability development, and consequently an energy cascade from large to small scales.

Decreasing the value of γ represents increasing turbulence lifetime, which increases the influence of curved trajectory on surface shear stress. With $\gamma \to \infty$, the turbulence decorrelation time scale approaches zero, meaning that the turbulence behaves like random molecular motion (i.e., the so-called statistically homogeneous and isotropic turbulence), and the traditional lower boundary condition is recovered. With $\gamma \ll 1$, the turbulence is characterized by a lifetime much longer than that in an idealized surface layer, presumably due to the presence of ABL-scale convective motions, surface heterogeneity, baroclinicity, or nonstationarity. The modified lower boundary condition has negligible influence on quasi-steady-state simulated tornadoes as long as the scale-analysis requirement $|\tau_n|/u_*^2 < 0.1$ holds over a relatively large fraction of the inner domain. Reducing the grid spacing broadens the flow types to which the modified lower boundary condition is applicable. Interestingly, simulations using the $(10\,\mathrm{m})^3$ grid spacing show that turbulence memory can significantly intensify a tornado before the central downdraft forms (which is a dynamic structure within a quasi-steady-state tornado).

The modified lower boundary condition is physically more realistic than the traditional lower boundary condition. The associated pathway of energy cascade is of potential relevance to LES without fully developed turbulent inflow conditions. Employing the modified lower boundary condition may significantly influence numerical simulations of cyclone intensification processes whose characteristic time scales are on the order of an hour or shorter. However, extending the formula proposed in section 2b to real atmospheric flows requires careful examination of each of the assumptions summarized in Table 1. Two key parameters for the modified lower boundary condition, α and γ, were prescribed as constants even though they are flow dependent. Estimating α and γ values requires novel approaches to reduce uncertainties in surface shear stress measurements and to quantify acceleration in the field.

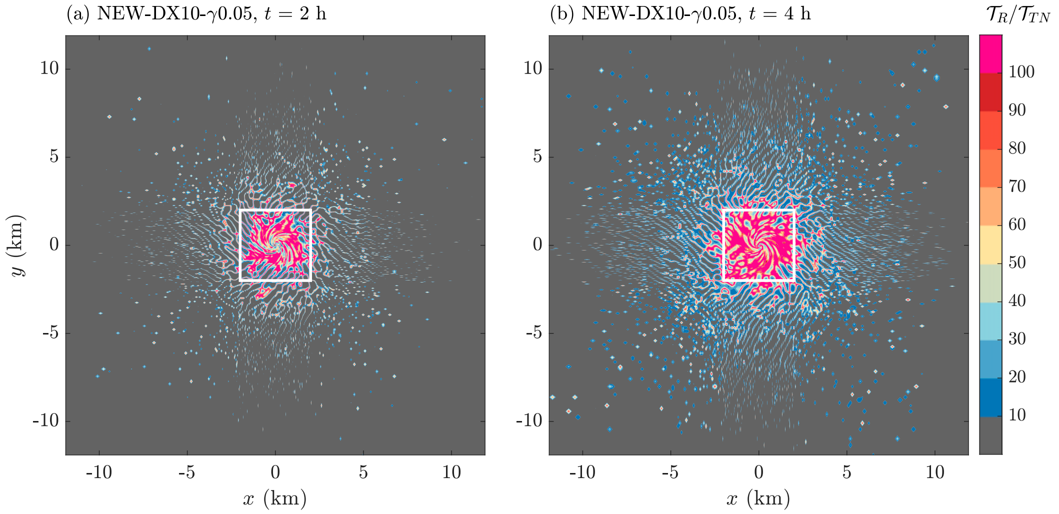

FIG. 11. As in Fig. 6, but for simulation NEW-DX10-γ0.05 at t = (a) 2 and (b) 4 h.

Last, turbulence memory is associated not only with curved trajectories, but also with longitudinal accelerations, and not only at the lower boundary, but also in the subgrid-scale motions in the interior of the flow. Future work will explore how best to include such effects. Ultimately, formulating and quantifying the rate of change of resolved shear on unresolved stress will require difficult-to-obtain field observations. Finally, quantifying the influences of any modified lower boundary condition on more realistic tornadoes, and possibly even tornadogenesis, will require numerical simulations with the parent storm and full representation of its microphysical processes.

Acknowledgments. Doctors George Bryan, Nathan Dahl, and David Nolan are acknowledged for their assistance throughout the course of this project. Special thanks are given to Dr. Bryan for his continued support of CM1. This work was funded by NSF Award AGS-1821885. We acknowledge high-performance computing support from Cheyenne (https://doi.org/10.5065/D6RX99HX) provided by NCAR's Computational and Information System Laboratory, sponsored by the National Science Foundation. Computations for this research were partially performed on the Pennsylvania State University's Institute for Computational and Data Sciences Roar supercomputer. We thank the three anonymous reviewers for constructive comments that have helped us to improve the paper.

Data availability statement. All simulation outputs created during this study are openly available from the Pennsylvania State University DataCommons (https://doi.org/10.26208/n95w-7r96).

APPENDIX

Implementation into CM1

CM1 employs a C-grid (Fig. A1), in which momentum budget terms for the horizontal velocity components ($\overline{u}$ and $\overline{v}$) are computed at U and V points, respectively. The traditional lower boundary condition [(12) and (13)] interpolates horizontal velocity components to Θ points to obtain $\overline{\mathbf{U}}_1$ and u_*; $\boldsymbol{\tau}_w$ is consequently at $z = 0$ at locations aligned horizontally with the Θ points. Last, τ_{xz} and τ_{yz} are computed at points aligned horizontally with U and V points, respectively, but at $z = 0$.

For the modified lower boundary condition [(44) and (45)], the longitudinal component (31) is computed using u_* provided by the traditional lower boundary condition, and the normal component (42) takes two prescribed parameters (α and γ), two time scales ($\mathcal{T}_{TN}$ and $\mathcal{T}_R$), and the direction of $\overline{\mathbf{U}}_1 \times \overline{\mathbf{a}}_1$. Computing $\mathcal{T}_{TN} = \kappa z_1/u_*$ is straightforward. Computing $\mathcal{T}_R$ given by (36) requires knowing the magnitude of $\overline{\mathbf{U}}_1 \times \overline{\mathbf{a}}_1$.

The CM1 governing equations for resolved horizontal motions are (Bryan 2017)

$$\begin{aligned}\overline{a}_x &= \frac{\overline{D}\,\overline{u}}{Dt} = \frac{\partial \overline{u}}{\partial t} - \mathrm{ADV}(\overline{u}) \\ &= -c_p\theta_\rho \frac{\partial \pi'}{\partial x} + f\overline{v} + T_{\overline{u}} + D_{\overline{u}} + N_{\overline{u}} \quad \text{and} \qquad , \\ \overline{a}_y &= \frac{\overline{D}\,\overline{v}}{Dt} = \frac{\partial \overline{v}}{\partial t} - \mathrm{ADV}(\overline{v}) = -c_p\theta_\rho \frac{\partial \pi'}{\partial y} - f\overline{u} + T_{\overline{v}} + D_{\overline{v}} + N_{\overline{v}}\end{aligned} \tag{A1}$$

where $\overline{a}_x$ and $\overline{a}_y$ are horizontal components of resolved acceleration, π is nondimensional pressure, θ_ρ is density potential temperature, c_p is specific heat of dry air, and f is the Coriolis parameter. Terms associated with ADV, T, D, and N represent net momentum fluxes due to resolved advection, unresolved turbulence, artificial diffusion, and Rayleigh damping, respectively. Turning on the budget-output option in CM1 enables computing all rhs terms in (A1),[A1] which are then combined to obtain $\overline{a}_x$ and $\overline{a}_y$ on U and V points, respectively.

[A1] The budget-output terms are computed at every time step, which requires a minor modification to the original CM1 code. Without this modification, the budget-output terms are computed at only output time steps.

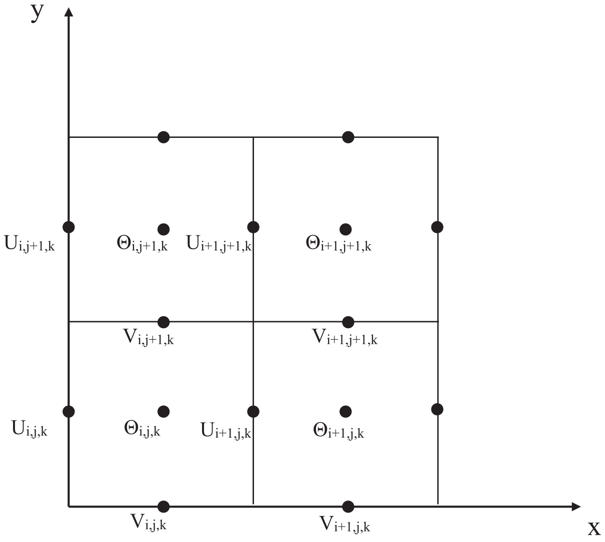

FIG. A1. The horizontal configuration of C-grid (vertically aligned with the first grid level of U, V, and Θ points).

Afterward, $\overline{a}_x$ and $\overline{a}_y$ at the first grid level are interpolated to Θ point to obtain $\overline{\mathbf{a}}_1$, where $\overline{\mathbf{U}}_1 \times \overline{\mathbf{a}}_1$ is computed. In summary, the modified lower boundary condition is computed at the same points as the traditional lower boundary condition.

REFERENCES

Bradshaw, P., and N. Pontikos, 1985: Measurements in the turbulent boundary layer on an 'infinite' swept wing. *J. Fluid Mech.*, **159**, 105–130, https://doi.org/10.1017/S0022112085003123.

Bryan, G. H., 2017: The governing equations for CM1. NCAR Doc., 24 pp., https://www2.mmm.ucar.edu/people/bryan/cm1/cm1_equations.pdf.

——, and H. Morrison, 2012: Sensitivity of a simulated squall line to horizontal resolution and parameterization of microphysics. *Mon. Wea. Rev.*, **140**, 202–225, https://doi.org/10.1175/MWR-D-11-00046.1.

——, N. A. Dahl, D. S. Nolan, and R. Rotunno, 2017: An eddy injection method for large-eddy simulations of tornado-like vortices. *Mon. Wea. Rev.*, **145**, 1937–1961, https://doi.org/10.1175/MWR-D-16-0339.1.

Burggraf, O. R., K. Stewartson, and R. Belcher, 1971: Boundary layer induced by a potential vortex. *Phys. Fluids*, **14**, 1821–1833, https://doi.org/10.1063/1.1693691.

Church, C., J. Snow, and E. Agee, 1977: Tornado vortex simulation at Purdue University. *Bull. Amer. Meteor. Soc.*, **58**, 900–908, https://doi.org/10.1175/1520-0477(1977)058<0900:TVSAPU>2.0.CO;2.

Davidson, P. A., 2015: *Turbulence: An Introduction for Scientists and Engineers*. 2nd ed. Oxford University Press, 629 pp.

Davies-Jones, R., 2015: A review of supercell and tornado dynamics. *Atmos. Res.*, **158–157**, 274–291, https://doi.org/10.1016/j.atmosres.2014.04.007.

——, R. J. Trapp, and H. B. Bluestein, 2001: Tornadoes and tornadic storms. *Severe Convective Storms, Meteor. Monogr.*, No. 50, Amer. Meteor. Soc., 167–221.

Deardorff, J. W., 1980: Stratocumulus-capped mixed layers derived from a three-dimensional model. *Bound.-Layer Meteor.*, **18**, 495–527, https://doi.org/10.1007/BF00119502.

Fiedler, B. H., 1995: On modelling tornadoes in isolation from the parent storm. *Atmos.–Ocean*, **33**, 501–512, https://doi.org/10.1080/07055900.1995.9649542.

——, and R. Rotunno, 1986: A theory for the maximum wind speeds in tornado-like vortices. *J. Atmos. Sci.*, **43**, 2328–2340, https://doi.org/10.1175/1520-0469(1986)043<2328:ATOTMW>2.0.CO;2.

Holton, J. R., and G. J. Hakim, 2013: *An Introduction to Dynamic Meteorology*. 5th ed. Elsevier Inc., 532 pp.

Kaimal, J. C., and J. J. Finnigan, 1994: *Atmospheric Boundary Layer Flows: Their Structure and Measurement*. Oxford University Press, 289 pp.

Lewellen, D., and W. Lewellen, 2007: Near-surface intensification of tornado vortices. *J. Atmos. Sci.*, **64**, 2176–2194, https://doi.org/10.1175/JAS3965.1.

Lewellen, W. S., 1976: Theoretical models of the tornado vortex. *Symp. on Tornadoes: Assessment of Knowledge and Implications for Man*, Lubbock, TX, Texas Tech. University, 107–143.

——, 1993: Tornado vortex theory. *The Tornado: Its Structure, Dynamics, Prediction, and Hazards, Geophys. Monogr.*, Vol. 79, Amer. Geophys. Union, 19–39.

Mahrt, L., D. Vickers, J. Sun, N. O. Jensen, H. Jørgensen, E. Pardyjak, and H. Fernando, 2001: Determination of the surface drag coefficient. *Bound.-Layer Meteor.*, **99**, 249–276, https://doi.org/10.1023/A:1018915228170.

Markowski, P. M., and G. H. Bryan, 2016: LES of laminar flow in the PBL: A potential problem for convective storm simulations. *Mon. Wea. Rev.*, **144**, 1841–1850, https://doi.org/10.1175/MWR-D-15-0439.1.

Moin, P., T.-H. Shih, D. Driver, and N. N. Mansour, 1990: Direct numerical simulation of a three-dimensional turbulent boundary layer. *Phys. Fluids*, **2**, 1846–1853, https://doi.org/10.1063/1.857658.

Monin, A. S., and A. M. Obukhov, 1954: Basic laws of turbulent mixing in the surface layer of the atmosphere. *Tr. Akad. Nauk SSSR Geophiz. Inst.*, **151**, 163–187.

Nolan, D. S., N. A. Dahl, G. H. Bryan, and R. Rotunno, 2017: Tornado vortex structure, intensity, and surface wind gusts in large-eddy simulations with fully developed turbulence. *J. Atmos. Sci.*, **74**, 1573–1597, https://doi.org/10.1175/JAS-D-16-0258.1.

Pan, Y., and E. G. Patton, 2017: On determining stationary periods within time series. *J. Atmos. Oceanic Technol.*, **34**, 2213–2232, https://doi.org/10.1175/JTECH-D-17-0038.1.

Poggi, D., A. Porporato, L. Ridolfi, J. D. Albertson, and G. G. Katul, 2004: The effect of vegetation density on canopy sublayer turbulence. *Bound.-Layer Meteor.*, **111**, 565–587, https://doi.org/10.1023/B:BOUN.0000016576.05621.73.

Pope, S. B., 2000: *Turbulent Flows*. Cambridge University Press, 771 pp.

Raupach, M. R., J. J. Finnigan, and Y. Brunet, 1996: Coherent eddies and turbulence in vegetation canopies: The mixing-layer analogy. *Bound.-Layer Meteor.*, **78**, 351–382, https://doi.org/10.1007/BF00120941.

Rotunno, R., 2013: The fluid dynamics of tornadoes. *Annu. Rev. Fluid Mech.*, **45**, 59–84, https://doi.org/10.1146/annurev-fluid-011212-140639.

——, G. H. Bryan, D. S. Nolan, and N. A. Dahl, 2016: Axisymmetric tornado simulations at high Reynolds number. *J. Atmos. Sci.*, **73**, 3843–3854, https://doi.org/10.1175/JAS-D-16-0038.1.

Schlichting, H., and K. Gersten, 2017: *Boundary-Layer Theory*. 9th ed. Springer, 805 pp.

Wyngaard, J. C., 2010: *Turbulence in the Atmosphere*. Cambridge University Press, 393 pp.